THE SECOND-ORDER HIGH FREQUENCY BISTATIC RADAR CROSS SECTION OF THE OCEAN SURFACE FOR "PATCH SCATTER"

WEIMIN HUANG

The Second-Order High Frequency Bistatic Radar Cross Section of the Ocean Surface for "Patch Scatter"

by

©Weimin Huang, B.Sc., M.Sc., Ph.D.

A thesis submitted to the School of Graduate Studies
in partial fulfillment of the requirements for the
degree of Master of Engineering

Faculty of Engineering and Applied Science
Memorial University of Newfoundland

February, 2004

St. John's Newfoundland

Your file Votre référence
ISBN: 0-612-99082-6
Our file Notre référence
ISBN: 0-612-99082-6

Abstract

The development of a model for the second-order bistatic HF radar cross section on an ocean surface patch remote from the transmitter and receiver is addressed. The cross section is referred to as patch scatter. The derivation starts with the second-order normal electric field equation which is in an asymptotic two-dimensional spatial-convolution form, and is accomplished by carrying out the inner convolution before its gradient. The bistatic result is verified by two means: (1) the complete form of the bistatic HF radar cross section in backscattering case is equivalent with the monostatic equation; (2) the bistatic electromagnetic coupling coefficient can be shown to reduce to the monostatic result when backscattering is imposed. The cross section model is also depicted and discussed based on simulation.

Acknowledgements

Before ending the documentation of this work, the author wishes to thank Dr. Gill and the Faculty of Engineering and Applied Science affording him the opportunity of continuing the study and research in this field. During the short two years, Dr. Gill showed impressive earnestness and patience in his supervision. His valuable suggestions act as a guiding light in the thick mist and his generous help comforts the author's living in St. John's. Furthermore, the author is grateful to graduate support from the School of Graduate Studies and a Natural Science and Engineering Research Council (NSERC) Grant to Dr. Eric Gill. Finally, appreciation should be given to the understanding and support of the author's wife, Yaying Tu, and family.

Contents

List of Figures

List of Symbols

The page numbers indicate the first significant reference to the symbol.

$(E_{0n}^{+})_1$: First-order of normal component of E_{0n}^{+}. (P.7)

k : Wavenumber of radar transmitted signal. (P.7)

C_0: Source-dependant constant in the temporal Fourier transform domain. (P.7)

$\xi(x,y)$: Two-dimensional ocean surface roughness. (P.7)

$F(\rho)$: Sommerfeld attenuation function with $\rho = \sqrt{x^2+y^2}$. (P.7)

$\overset{xy}{*}$: Two-dimensional spatial convolution symbol. (P.7)

$\sigma_1(\omega_d)$: First-order Doppler cross section per unit area of surface. (P.7)

ω_d: Doppler frequency. (P.7)

$K_0(=\frac{\omega_0}{c})$: Wavenumber of the dipole excitation current. (P.7)

$\Delta\rho_s(=\frac{c\tau_0}{2})$: Patch width as viewed by pulse radar. (P.7)

$S(\vec{K},\omega)$: Ocean surface waveheight spectrum. (P.7)

$\vec{K}$: Surface wave vector of magnitude K and planar components K_x and K_y. (P.7)

ϕ_0 : Representative value of the bistatic angle. (P.7)

g : Gravitational acceleration. (P.7)

$Sa(\cdot)$: Sampling function. (P.7)

$(E_{0n}^{+})_2$: Second-order of normal component of E_{0n}^{+}. (P.9)

$\vec{\rho}_1$: Displacement from the transmitter to the first scatter point. (P.14)

$\vec{\rho}_{12}$: Displacement from the first scatter point to the second

scatter point. (P.14)

P_{mn} : Fourier coefficient of a surface component whose wave vector is $\vec{K}_{mn} = Nm\hat{x} + Nn\hat{y}$. (P.14)

θ_{mn} : Direction of $\vec{K}_{mn}$. (P.14)

θ : Direction of $\vec{\rho}$ as measured from transmitter to receiver. (P.14)

θ_1 : Direction of $\vec{\rho}_1$. (P.14)

$\vec{\rho}_2$: Displacement from the transmitter to the second scatter point. (P.15)

θ_2 : Direction of $\vec{\rho}_2$. (P.15)

(μ, δ) : Elliptical coordinates. (P.15)

$\vec{K}_{pq}$: Wave vector of surface component analogous to $\vec{K}_{mn}$. (P.20)

P_{pq} : Fourier coefficient of a surface component whose wave vector is $\vec{K}_{pq}$. (P.20)

θ_{pq} : Direction of $\vec{K}_{pq}$. (P.20)

$\vec{K}_{rs}$: Sum $(\vec{K}_{mn} + \vec{K}_{pq})$ of the scattering wave vectors whose direction is θ_{rs}. (P.22)

$\vec{\rho}_{20}$: Displacement from the second scatter point to the receiver. (P.22)

ϕ : Bistatic angle. (P.25)

ρ_{s21} : $= \dfrac{\rho_2 + \rho_{20}}{2}$. (P.25)

t : Time variable. (P.27)

$\mathcal{F}_t, \mathcal{F}_t^{-1}$: Temporal Fourier transform and its inverse. (P.27)

ω_0 : Angular frequency of a pulsed sinusoid. (P.27)

ω : Angular frequency of the electric field. (P.27)

$\delta(\cdot)$: Dirac delta function. (P.27)

c : Free-space speed of light. (P.27)

η_0 : Intrinsic impedance of free space. (P.27)

$\Delta\ell$: Length of vertical dipole. (P.27)

$I(\omega)$: Arbitrary source current. (P.27)

$i(t)$: Source current in the time domain. (P.28)

τ_0 : Transmit pulse length. (P.28)

$h(\cdot)$: Heaviside function. (P.28)

I_0 : Peak current on a pulsed dipole. (P.28)

θ_N : Ellipse normal direction. (P.30)

Γ_{EP}: Electromagnetic coupling coefficient. (P.31)

$P_{\vec{K},\omega}$: Random Fourier coefficient of the surface associated with the component whose wave vector is $\vec{K}$ and whose angular frequency is ω. (P.35)

Γ_H: Hydrodynamic coupling coefficient. (P.35)

Γ_P: Total coupling coefficient. (P.36)

ω_1, ω_2 : Angular frequency of the first- and second ocean waves. (P.36)

$< \cdot >$: Ensemble average. (P.37)

$R(\tau)$: Autocorrelation of the received electric field. (P.37)

A_r: Effective free space aperture of the receiving antenna. (P.37)

λ_0 : Wavelength of radar transmitted signal. (P.37)

G_r: Free space gain of the receiving antenna. (P.37)

N : Fundamental surface wavenumber. (P.37)

W : Fundamental surface angular frequency. (P.37)

m_1, m_2: Indicators for Doppler frequency region for second-order cross section. (P.39)

$P(\omega_d)$: Doppler power spectral density of the received electric field where ω_d is the Doppler frequency. (P.40)

dA: Elementary area of scatter surface. (P.40)

P_t: Transmitted power. (P.42)

G_t: Free space gain of the transmitting antenna. (P.42)

$\sigma_{2P}(\omega_d)$: Second-order Doppler cross section per unit area of surface. (P.42)

$\vec{N}, \vec{T}$: Normal and tangent vectors, respectively, to the scatter ellipse, and θ_N is the direction of $\vec{N}$. (P.45)

$g(\theta_{\vec{K}})$: Directional characteristic of the ocean surface. (P.50)

U_W : Wind speed. (P.50)

$s(K)$: Spreading factor for the ocean wave directional characteristic. (P.50)

φ_W: Mean wind direction. (P.50)

$\Gamma(\cdot)$: Gamma function. (P.51)

U_{10} : Wind speed 10 m over the ocean surface. (P.51)

R: Logarithm ratio of the right Bragg peak to the left one. (P.54)

θ_W: Angle between the radar beam and the mean wind direction. (P.54)

f_0: Frequency of the radar transmitted signal. (P.59)

f_B: Bragg frequency. (P.59)

λ_B : Wavelength of Bragg wave. (P.60)

λ : Wavelength of ocean wave. (P.63)

Chapter 1

Introduction

1.1 Background of Study

The ocean covers about seventy-one percent of the earth. The conditions at sea not only affect the local and global weather, but also influence human activities (fisheries, rescue at sea and national defense). More than one hundred coastal nations currently have economic jurisdiction up to the 200-nautical-mile (nm) limit under the terms of the United Nations Convention on the Law of the Sea (UNCLOS). Coastal nations are encouraged to monitor their adjoining maritime zones.

The usual tools used to observe the ocean are weather maps, buoys, microwave radars and satellites [1]–[3]. However, they have limited observing area or accuracy. Weather maps can only provide qualitative analysis. Though buoys can provide in-situ data and have relatively better accuracy, they can be easily destroyed and can't collect sea surface information over large areas. Microwave radar is limited to line-of-sight measurement. Even though satellites can cover large areas, their

repeat times may be several days, and they are therefore not suited for continuous coverage in time.

In 1955, Crombie [4] properly attributed the dominant features of high frequency (HF) Doppler spectra associated with ocean backscatter as Bragg scatter. The development of the first HF radar cross sections of the ocean by Barrick [5], [6] led almost immediately to the recognized potential of HF radar for the remote sensing of sea surface parameters such as current velocity and wave and wind fields over large maritime regions. It can also be used to detect and track surface targets and effectively monitor surface vessels which may be involved in activities such as drug trafficking, smuggling, piracy, illegal fishing and unlawful immigration. Data from HF radars has been used in tracking icebergs, and for search and rescue operations.

Land-based HF radar can provide continuous, all-weather and real-time surveillance of Exclusive Economic Zone (EEZ) waters at a fraction of the cost of traditional methods. The capacity to make such surveillance over very large regions on reasonable temporal and spatial scales has obvious implications for a variety of scientific, industrial and enforcement endeavours. For homeland security, the Canadian goverment will spend 50 million dollars to install a new military radar network on the East and West coast to track everything from terrorists trying to slip into the country in small boats to illegal foreign fishing fleets. These radars will also provide data which can be used to determine sea surface parameters such as current vectors, waveheight spectra and wind direction.

1.2 Review of Literature

For more than two decades, many successful measurements of ocean surface parameters and moving targets by HF radars operating at 3-30 MHZ have been reported (see, for example, [7]–[49]). HF radars work in sky-wave or ground-wave mode. Sky-wave radars, whose radio wave travels upward from the antenna and may be reflected to earth by the ionosphere, can be used to make large spatial scale measurements (e.g., [7]–[14], [20]–[25]). Ground-wave radars, whose signal follows the curvature of the earth for some distance, are still an important area of research (see, for example, [19], [26]–[38], [40]–[43], [45]–[48]).

Most of the initial work was carried out based on Barrick's HF radar cross sections of the ocean surface [5], [6]. However, Barrick's formulations are focused primarily on the case of co-location of transmitter and receiver - i.e. monostatic (or backscatter) operation. Figure 1.1 shows the monostatic geometry. In general, wind and wave directions remotely sensed with a single monostatic radar involve an ambiguity [8], [29], [39], [41]. This arises because waves coming from left and right at the same angle relative to the radar beam will produce the same Doppler spectrum. In order to remove the ambiguity, additional constraints (e.g., the fact that winds blow anti-clockwise around a low-pressure center in the North Hemisphere) or a second monostatic radar must be used [29], [47]. It is difficult to apply meteorological knowledge to resolve the wind directional ambiguity for ground-wave radars [29]. In using two radars (dual-station), site selection and availability, the added costs of an extra station, and the difficulty of optimal antenna deployment for maximum side-lobe reduction are usually limitations which must be addressed. Recently, some researchers (e.g., [39], [41], [47]) have presented

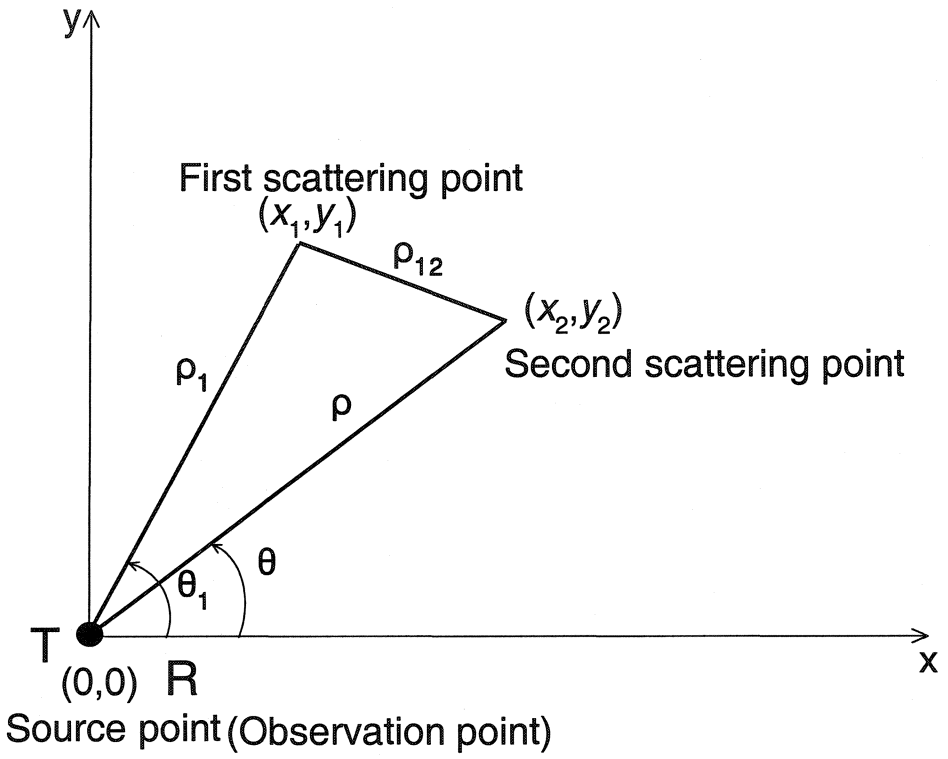

Figure 1.1: Monostatic scatter geometry

excellent work on factors to be considered in developing improved algorithms for the extraction of unambiguous wind direction from HF and VHF Doppler spectra under monostatic operation. However, problems still exist in finding wave direction using a single monostatic radar. Thus, more and more attention [50]–[57] is being paid to bistatic radars for which the transmitter and receiver are not co-located (as shown in Figure 1.2). From this perspective, the analysis of the bistatic radar cross sections is of much importance.

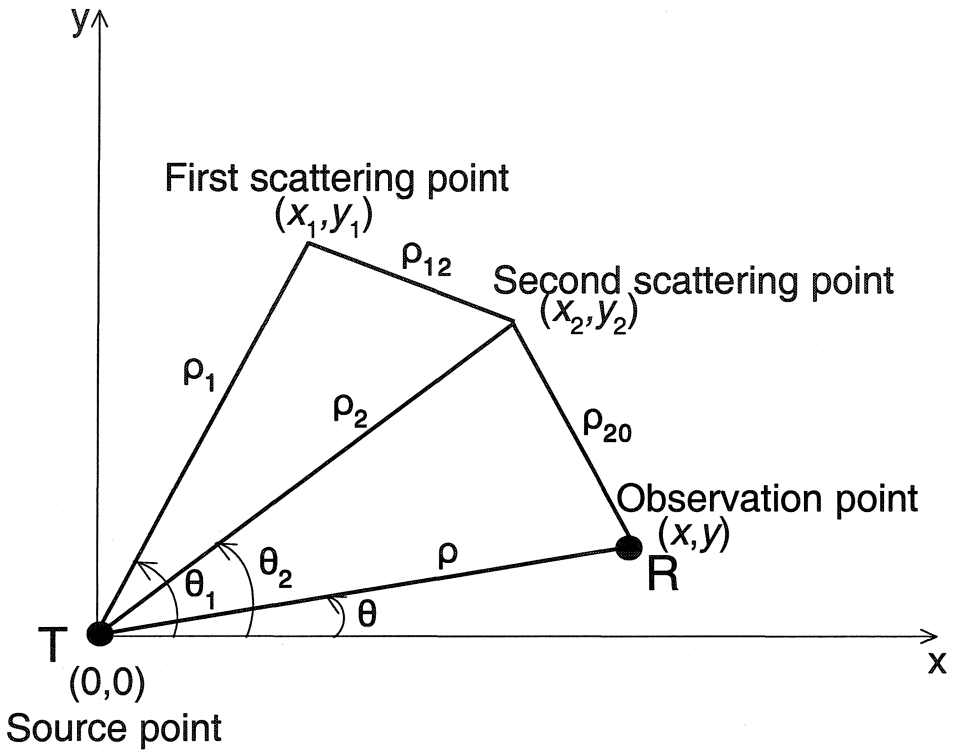

Figure 1.2: Bistatic scatter geometry

In order to derive the bistatic HF radar cross section of the ocean surface, the problem of the scattering of electromagnetic (e-m) wave energy from rough surfaces must be considered.

In 1896, Lord Rayleigh [58] applied the perturbation method to the scattering of acoustical signals from rough surfaces, and in 1951 Rice [59] applied it in analogous electromagnetic problems. This approach was later used by Wait [60] and Barrick [61], [62] in addressing a variety of e-m scattering problems. Thirty

years ago, Barrick [5], [6] deduced the first-order and second-order monostatic HF radar cross sections for the ocean surface scattering. The basic requirements in the application of the perturbation method are that the surface profile variations be small compared to the radio wavelength and the surface slopes be much smaller than unity.

In 1980, Walsh [63] proposed an alternate technique (generalized function approach) for the study of rough surface propagation and scatter. Because of its relevance to this thesis, the results of Walsh's work are considered in some detail here. Walsh's method is based on a decomposition of surface characteristics and e-m field components in terms of the Heaviside function to specify the various regions of the total scattering space. As noted in [64], [65] his technique contains a minimum of sophisticated analysis and has the following properties: (1) The analysis proceeds directly from Maxwell's equations; (2) the source field is arbitrary; (3) the boundary conditions are generated naturally from the initial formulation of the problem. The method has been successfully used to study the problem of propagation and scattering for mixed paths with discontinuities [66] and periodic surfaces [67]. In 1987, Walsh and Donnelly [68] developed new, general expressions for the normal and tangential electric field for a surface with arbitrary profile. By imposing conditions of a good conducting surface and small surface height variations compared to the radio wavelength, a general series solution of the normal electric field component up to third-order was derived for the scattering surface representable as a Fourier series with a vertical dipole radiation source [69]. Srivastava [70] produced the first HF monostatic cross section of the ocean using Walsh's theory.

The first-order bistatically-observed normal electric field is given in [69] as

$$(E_{0n}^{+})_1 \approx -jkC_0 \left[\hat{\rho} \cdot \nabla_{xy}(\xi) F(\rho) \frac{e^{-jk\rho}}{2\pi\rho} \overset{xy}{*} F(\rho) \frac{e^{-jk\rho}}{2\pi\rho} \right] \tag{1.1}$$

where C_0 is a source-dependent constant in the temporal Fourier transform domain, k is the wave number of the transmitted signal, $\xi(x, y)$ describes a two-dimensional rough surface, $F(\rho)$ is the Sommerfeld attenuation function, $\rho = \sqrt{x^2 + y^2}$, and $\overset{xy}{*}$ represents a two-dimensional spatial convolution symbol. The first-order field is associated with a single electromagnetic scatter from the surface. In the development of the first-order radar cross section model, a "narrow beam" receive system is assumed. The basic scattering analysis is not restricted to the type of modulation, but the radar cross section derivation here assumes a pulse dipole source. The radar cross section of the ocean is derived in the "ensemble average" sense by considering that the ocean surface variations may be modeled as a zero-mean Gaussian process. The ocean surface was assumed to be slightly rough and good conducting. With reference to Figure 1.3, the first-order HF bistatic Doppler radar cross section per unit area was derived as [50]:

$$\begin{aligned} \sigma_1(\omega_d) &= 2^4 \pi K_0^2 \Delta\rho_s \sum_{m=\pm 1} S(m\vec{K}) \frac{K^{5/2} \cos\phi_0}{\sqrt{g}} \\ &\quad \cdot Sa^2 \left[\frac{\Delta\rho_s}{2} \left(\frac{K}{\cos\phi_0} - 2K_0 \right) \right] \end{aligned} \tag{1.2}$$

The various quantities associated with (1.2) are given below:

$\omega_d \equiv$ Doppler frequency

$K_0 \equiv$ radio wave wavenumber

$\Delta\rho_s \equiv$ range resolution or patch width

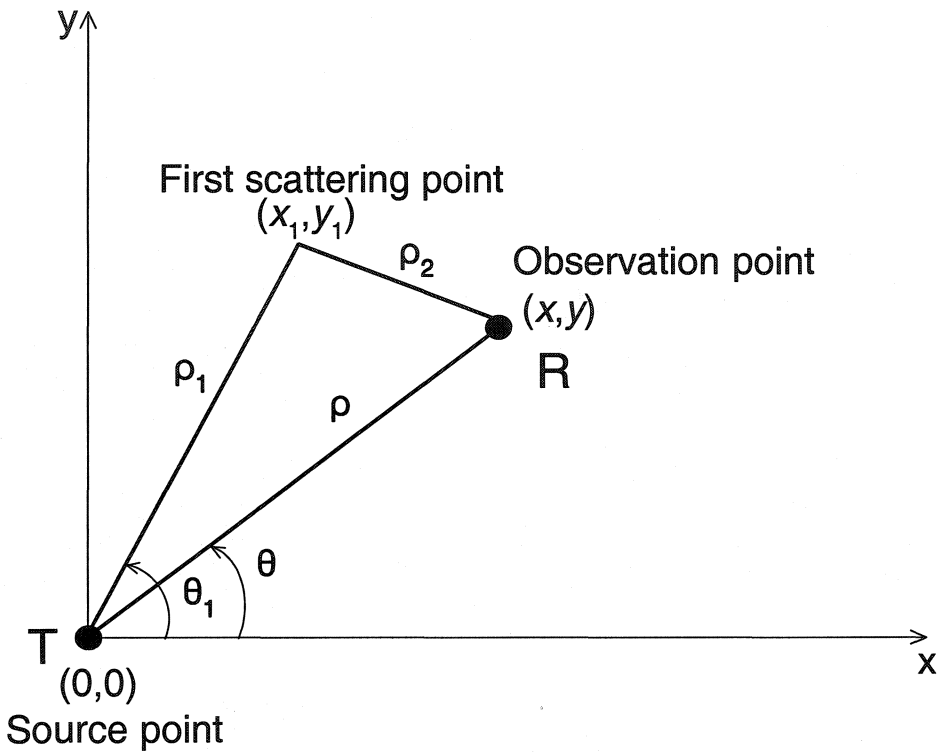

Figure 1.3: First-order bistatic scatter geometry

$S(\vec{K}) \equiv$ directional (two-dimension) ocean waveheight spectrum

$K(= \omega_d^2/g) \equiv$ the ocean wavenumber, and g is gravitational acceleration

$Sa(x) \equiv \dfrac{\sin x}{x}$

$\phi_0 \equiv$ half angle between transmitter and receiver as seen from scattering patch – i.e. the bistatic angle

Obviously, the first-order cross section depends on the patch width, and it establishes a rapid oscillating first-order continuum in addition to the sharp primary

Bragg peaks because of the $Sa^2()$ factor. Furthermore, the first-order bistatic HF radar cross section of the ocean surface was shown to reduce to Barrick's result when the patch width $\Delta\rho_s$ becomes unbounded [50], [51]. In that case, the sampling squared function is replaced by a delta function.

The second-order normal electric field has the form [69]

$$\begin{aligned}(E_{0n}^{+})_2 \approx\ & -jkC_0\{\nabla_{xy}(\xi) \\ & \cdot\nabla_{xy}\left[\hat{\rho}\cdot\nabla_{xy}(\xi)F(\rho)\frac{e^{-jk\rho}}{2\pi\rho} \overset{xy}{*} F(\rho)\frac{e^{-jk\rho}}{2\pi\rho}\right] \\ & \overset{xy}{*} F(\rho)\frac{e^{-jk\rho}}{2\pi\rho}\Bigg\}\end{aligned} \tag{1.3}$$

The meaning of each term in (1.3) will be discussed in detail in the following chapter. Here, interest is paid only to its form. It is an asymptotic two-dimensional spatial-convolution equation. This expression has been used to develop the second-order bistatic HF radar cross section of the ocean surface [53]–[55]. When deriving the second-order cross section from (1.3), Gill [53] used the identity

$$\begin{aligned}\nabla_{xy}(A \overset{xy}{*} B) &= A \overset{xy}{*} \nabla_{xy}(B) \\ &= B \overset{xy}{*} \nabla_{xy}(A)\end{aligned} \tag{1.4}$$

and carried out the inner convolution after its gradient. He found that the second-order scatter field consists of three significant terms: (1) two scatters occur on a patch of surface remote from both the transmitter and receiver (that patch being the same as for the single, first-order scatter); (2) a single scatter near the transmitter followed by another on the remote patch before reception; and (3) a first scatter on the remote patch followed by another at the receiver immediately

prior to reception. These cross sections provide the necessary models for the future bistatic operation of HF radars in a coastal setting.

1.3 Scope of Thesis

While Gill's approach [53] led to a more general result than previous work, it precluded the possibility of comparing the newly-derived bistatic patch-scatter cross sections with the monostatic counterpart already developed using the same theory [69]. This fact rested entirely on the order in which the gradient and convolution referred to above were carried out. In this thesis, the question, "If the identity of (1.4) is not deployed in (1.3), what will the result be?", is posed. Prompted by this question and based on the normal component of the surface wave field for a vertical dipole source developed by Walsh *et al.* [69], the second-order bistatic HF radar cross section of the ocean surface is established by carrying out the inner convolution before its gradient in equation (1.3). In the development of the radar cross section model, a "narrow beam" receive system and deep water are assumed. The result allows direct comparison with existing monostatic models when the relevant geometry is introduced.

In Chapter 2, the normal component of the surface wave field equation for the second-order scatter from a time-invariant surface representable by a Fourier series is examined. With small surface slope, small height and a vertical dipole source, a solution for the field equation is approximated via the stationary phase method.

The second-order bistatic HF radar cross section of the ocean surface patch scatter is developed in Chapter 3. The result is shown to contain the classical

monostatic radar cross section. This is verified from both the structure of the bistatic equation form and the particular electromagnetic coupling coefficient for the monostatic case.

In Chapter 4, the bistatic radar cross sections for patch scatter are simulated using the Pierson-Moskowitz model with a cardioid directional distribution for the directional ocean wave height spectrum of a wind-driven sea. Their properties and dependence on ocean conditions are compared and discussed.

Finally, Chapter 5 offers some concluding remarks and lists some related future work.

Chapter 2

The Second-order Bistatic Electric Field Solution for "Patch Scatter" from a Time-invariant Surface

The second-order field consists of a double electromagnetic scatter from first-order surface waves [50], [51]. As shown in Figure 2.1, the radiation from the radar transmitter position $T(0,0)$ scatters in all directions from a general point (x_1, y_1). Some of the energy scatters again at point (x_2, y_2), and a portion of this is received at $R(x,y)$. The expression for the second-order field, $(E_{0n}^{+})_2$, derived by Walsh and Gill [64] is

$$(E_{0n}^{+})_2 \approx -jkC_0 \left\{ \nabla_{xy}(\xi) \right.$$

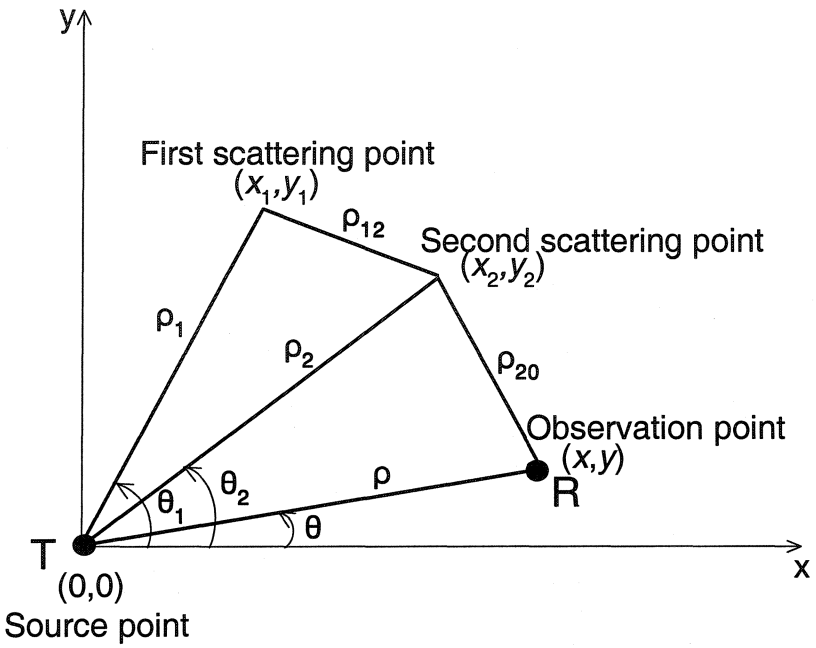

Figure 2.1: Second-order bistatic scatter geometry

$$\cdot\nabla_{xy}\left[\hat{\rho}\cdot\nabla_{xy}(\xi)F(\rho)\frac{e^{-jk\rho}}{2\pi\rho}\overset{xy}{*}F(\rho)\frac{e^{-jk\rho}}{2\pi\rho}\right]\overset{xy}{*}F(\rho)\frac{e^{-jk\rho}}{2\pi\rho}\Bigg\} \tag{2.1}$$

where ∇_{xy} is the planar gradient. The surface $\xi(x,y)$ or $\xi(\rho,\theta)$ from which the radiation is scattered can be represented by a two-dimensional Fourier series. The $F()$ is the usual Sommerfeld attenuation function. The field scattering from (x_1,y_1) and reaching (x_2,y_2) is represented by the inner convolution of equation (2.1). The dot product of the gradient (∇_{xy}) of this convolution with the surface gradient $(\nabla_{xy}(\xi))$ represents the scatter from (x_2,y_2). The final convolution gives the

received field at $R(x,y)$. Therefore, equation (2.1) includes two scatters from any and all points on the surface.

2.1 Stationary Phase Integration of the Inner Convolution

Now, consider the inner convolution in equation (2.1) with Figure 2.1 and let

$$\begin{aligned} I_1 &= \hat{\rho}\cdot\nabla_{xy}(\xi)F(\rho)\frac{e^{-jk\rho}}{2\pi\rho} \overset{xy}{*} F(\rho)\frac{e^{-jk\rho}}{2\pi\rho} \\ &= \frac{1}{(2\pi)^2}\int_{x_1}\int_{y_1}\left[\hat{\rho}\cdot\nabla_{xy}(\xi)\right]F(\rho_1)F(\rho_{12})\frac{e^{-jk(\rho_1+\rho_{12})}}{\rho_1\rho_{12}}dx_1dy_1 \end{aligned} \tag{2.2}$$

The surface where the first scatter happens can be represented as Fouier series

$$\begin{aligned} \xi(x,y) &= \sum_{mn} P_{mn}e^{jN(mx+ny)} \\ &= \sum_{mn} P_{mn}e^{j\vec{\rho}\cdot\vec{K}_{mn}} \\ &= \sum_{mn} P_{mn}e^{j\rho K_{mn}\cos(\theta_{mn}-\theta)} \end{aligned} \tag{2.3}$$

where $\vec{K}_{mn} = (K_{mn}, \theta_{mn})$ is the surface wave vector of magnitude K_{mn} and direction θ_{mn}, P_{mn} is the Fourier coefficient. Using $\nabla_{xy} = \hat{\rho}\dfrac{\partial}{\partial\rho} + \hat{\theta}\dfrac{1}{\rho}\dfrac{\partial}{\partial\theta}$ gives

$$\hat{\rho}\cdot\nabla_{xy}(\xi) = j\sum_{mn} P_{mn}K_{mn}\cos(\theta_{mn}-\theta)e^{j\rho K_{mn}\cos(\theta_{mn}-\theta)} \tag{2.4}$$

Inserting (2.4) into (2.2) gives

$$I_1 = \frac{j}{(2\pi)^2}\sum_{mn} P_{mn}K_{mn}\cdot\int_{x_1}\int_{y_1}\cos(\theta_{mn}-\theta_1)$$

$$\cdot e^{j\rho_1[K_{mn}\cos(\theta_{mn}-\theta_1)-k]-jk\rho_{12}}\frac{F(\rho_1)F(\rho_{12})}{\rho_1\rho_{12}}dx_1dy_1 \tag{2.5}$$

The method of two-dimensional stationary phase [71] may be applied to (2.5). However, the term $\rho_1\rho_{12}$ will violate the required assumption of "slowly varying" with respect to the exponential. In order to alleviate this problem, a transformation of coordinates may be effected as follows:

(1) rotation of the axes by θ_2, i.e.,

$$\begin{aligned} x_1 &= x_1^{'}\cos\theta_2 - y_1^{'}\sin\theta_2 \\ y_1 &= x_1^{'}\sin\theta_2 + y_1^{'}\cos\theta_2 \end{aligned} \tag{2.6}$$

(2) shift of the origin in the $(x_1^{'}, y_1^{'})$ plane to a position halfway along ρ_2,

$$\begin{aligned} x_1^{''} &= x_1^{'} - \frac{\rho_2}{2} \\ y_1^{''} &= y_1^{'} \end{aligned} \tag{2.7}$$

then

$$\begin{aligned} x_1 &= \left(x_1^{''} + \frac{\rho_2}{2}\right)\cos\theta_2 - y_1^{''}\sin\theta_2 \\ y_1 &= \left(x_1^{''} + \frac{\rho_2}{2}\right)\sin\theta_2 + y_1^{''}\cos\theta_2 \end{aligned} \tag{2.8}$$

(3) conversion to elliptic coordinates (μ, δ),

$$\begin{aligned} x_1^{''} &= \frac{\rho_2}{2}\cosh\mu\cos\delta \\ y_1^{''} &= \frac{\rho_2}{2}\sinh\mu\sin\delta \end{aligned} \tag{2.9}$$

According to the complete transformation,

$$\begin{aligned} x_1 &= \frac{\rho_2}{2}[(1+\cosh\mu\cos\delta)\cos\theta_2 - \sinh\mu\sin\delta\sin\theta_2] \\ y_1 &= \frac{\rho_2}{2}[(1+\cosh\mu\cos\delta)\sin\theta_2 + \sinh\mu\sin\delta\cos\theta_2] \end{aligned} \tag{2.10}$$

It is easy to determine that

$$\begin{aligned} \rho_1 &= \sqrt{x_1^2+y_1^2} \\ &= \frac{\rho_2}{2}(\cosh\mu+\cos\delta), \end{aligned} \tag{2.11}$$

$$\begin{aligned} \rho_{12} &= \sqrt{(x_2-x_1)^2+(y_2-y_1)^2} \\ &= \frac{\rho_2}{2}(\cosh\mu-\cos\delta), \end{aligned} \tag{2.12}$$

and

$$\begin{aligned} \theta_1 &= \tan^{-1}\left(\frac{y_1}{x_1}\right) \\ &= \tan^{-1}\left[\frac{(1+\cosh\mu\cos\delta)\sin\theta_2+\sinh\mu\sin\delta\cos\theta_2}{(1+\cosh\mu\cos\delta)\cos\theta_2-\sinh\mu\sin\delta\sin\theta_2}\right] \end{aligned} \tag{2.13}$$

By using these transformations, equation (2.5) may be written as

$$\begin{aligned} I_1 = {} & \frac{j}{(2\pi)^2}\sum_{mn} P_{mn}K_{mn} \\ & \cdot\int_0^{\pi}\int_{-\infty}^{\infty}\cos(\theta_{mn}-\theta_1)F(\rho_1)F(\rho_{12}) \\ & \cdot e^{j(\rho_2/2)K_{mn}[(1+\cosh\mu\cos\delta)\cos(\theta_{mn}-\theta_2)+\sinh\mu\sin\delta\sin(\theta_{mn}-\theta_2)]-2k\cosh\mu} \\ & \cdot d\mu d\delta \end{aligned} \tag{2.14}$$

In order to determine the stationary points of (2.14) (see equation (A.2)), the function appearing in the exponent, given as

$$\begin{aligned}\phi(\mu,\delta) &= K_{mn}[(1+\cosh\mu\cos\delta)\cos(\theta_{mn}-\theta_2) \\ &\quad +\sinh\mu\sin\delta\sin(\theta_{mn}-\theta_2)] - 2k\cosh\mu, \end{aligned} \tag{2.15}$$

must be examined.

The condition for a two-dimensional stationary point requires

$$\begin{aligned}\frac{\partial\phi}{\partial\mu} &= K_{mn}[\sinh\mu\cos\delta\cos(\theta_{mn}-\theta_2) \\ &\quad +\cosh\mu\sin\delta\sin(\theta_{mn}-\theta_2)] - 2k\sinh\mu = 0 \\ \frac{\partial\phi}{\partial\delta} &= K_{mn}[-\cosh\mu\sin\delta\cos(\theta_{mn}-\theta_2) \\ &\quad +\sinh\mu\cos\delta\sin(\theta_{mn}-\theta_2)] = 0 \end{aligned} \tag{2.16}$$

The interesting stationary points are given by

$$\sinh\mu = 0, \sin\delta = 0 \tag{2.17}$$

or

$$\mu = 0, \delta = 0, \pm\pi \tag{2.18}$$

In particular, the point $(\mu,\delta) = (0,0)$ satisfies

$$\begin{aligned}\rho_{12} &= \frac{\rho_2}{2}(\cosh\mu - \cos\delta) = 0 \\ \rho_1 &= \frac{\rho_2}{2}(\cosh\mu + \cos\delta) = \rho_2 \end{aligned} \tag{2.19}$$

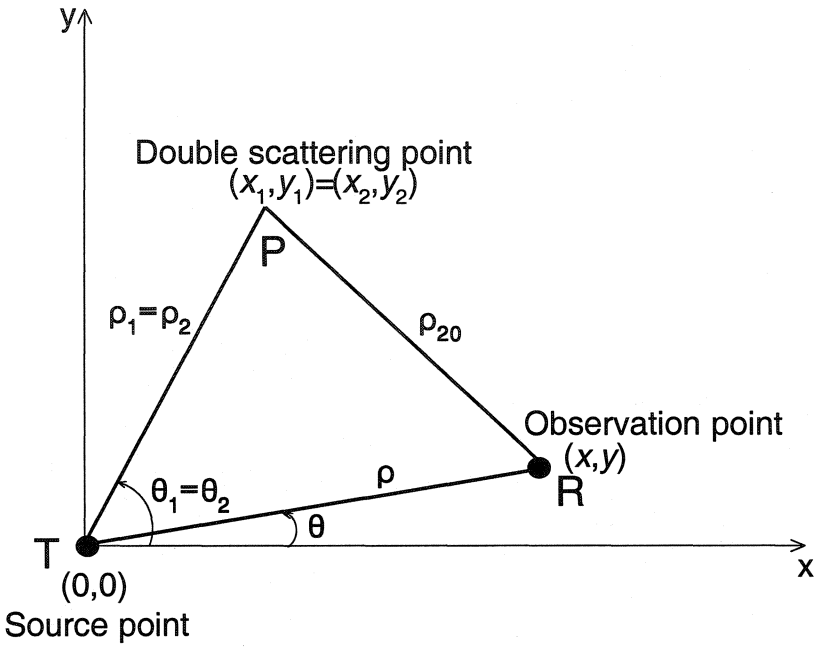

Figure 2.2: Geometry of the bistatic patch scatter

This indicates a double scatter at (x_1, y_1) (i.e., $(x_2, y_2) = (x_1, y_1)$) and $\theta_1 = \theta_2$ (as shown in Figure 2.2). This has been called "patch scatter" when this analysis is applied to a pulse radar. It happens over a finite illuminated area and is of much interest. Thus, the effect of the finite patch scattering may not be negligible. Other investigators [70], [53] have shown that the patch-scatter phenomenon dominates other effects almost everywhere in the Doppler spectrum. For this reason, only the patch scatter condition, i.e. the (0,0) stationary point, is addressed in this work.

According to the stationary theory, the determinant of the matrix,

$$\phi_{\mu\delta}(\mu,\delta) = \begin{pmatrix} \frac{\partial^2\phi}{\partial\mu^2} & \frac{\partial^2\phi}{\partial\mu\partial\delta} \\ \frac{\partial^2\phi}{\partial\delta\partial\mu} & \frac{\partial^2\phi}{\partial\delta^2} \end{pmatrix} \tag{2.20}$$

is required at the stationary point (0,0). It is easy to deduce

$$\begin{aligned} \phi_{\mu\delta}(0,0) &= \begin{pmatrix} K_{mn}\cos(\theta_{mn}-\theta_2)-2k & K_{mn}\sin(\theta_{mn}-\theta_2) \\ K_{mn}\sin(\theta_{mn}-\theta_2) & -K_{mn}\cos(\theta_{mn}-\theta_2) \end{pmatrix} \\ &= 2kK_{mn}\cos(\theta_{mn}-\theta_2) - K_{mn}^2 \end{aligned} \tag{2.21}$$

In addition

$$\phi(0,0) = 2K_{mn}\cos(\theta_{mn}-\theta_2) - 2k \tag{2.22}$$

is required. Meanwhile,

$$Sig(\phi_{\mu\delta}(0,0)) = -2 \tag{2.23}$$

where $Sig()$ =(number of positive eigenvalues)-(number of negative eigenvalues).

By using the results of (2.21)–(2.23) and stationary phase theory (Appendix A), equation (2.14) may be evaluated asymptotically (i.e. for large $\rho_2 K_{mn}$), with the first and second scattering points at one patch satisfying $\theta_1 = \theta_2, F(\rho_{12}) = F(0) = 1$, to give

$$\begin{aligned} I_1 \approx\ & jF(\rho_2)\frac{e^{-jk\rho_2}}{2\pi\rho_2}\sum_{mn} P_{mn}\cdot\frac{K_{mn}\cos(\theta_{mn}-\theta_2)}{\sqrt{K_{mn}^2-2kK_{mn}\cos(\theta_{mn}-\theta_2)}} \\ & \cdot e^{j\rho_2 kK_{mn}\cos(\theta_{mn}-\theta_2)} \end{aligned} \tag{2.24}$$

Recalling the definition of I_1 in equation (2.2) and using (2.24), equation (2.1) becomes

$$\begin{aligned}(E_{0n}^{+})_2 \approx & -jkC_0 \Bigg\{ \nabla_{xy}(\xi) \cdot \nabla_{xy} \Bigg[jF(\rho) \frac{e^{-jk\rho}}{2\pi\rho} \\ & \cdot \sum_{mn} P_{mn} e^{j\rho K_{mn} \cos(\theta_{mn}-\theta)} \\ & \cdot \frac{K_{mn}\cos(\theta_{mn}-\theta)}{\sqrt{K_{mn}^2 - 2kK_{mn}\cos(\theta_{mn}-\theta)}} \Bigg] \\ & \overset{xy}{*} F(\rho) \frac{e^{-jk\rho}}{2\pi\rho} \Bigg\} \end{aligned} \tag{2.25}$$

2.2 Solving the Outer Convolution

The geometry described by (2.25) is given in Figure 2.2 which is similar to Figure 2.1. The surface at the second scattering point may be written similarly as equation (2.3) in the form

$$\begin{aligned}\xi(x,y) &= \sum_{pq} P_{pq} e^{j\vec{\rho}\cdot\vec{K}_{pq}} \\ &= \sum_{pq} P_{pq} e^{j\rho K_{pq}\cos(\theta_{pq}-\theta)} \end{aligned} \tag{2.26}$$

Again using the polar representation of ∇_{xy} and dropping terms with order of $1/\rho$ which are greater or equal to 2, the inner gradient of equation (2.25) may be approximated as

$$\begin{aligned}\nabla_{xy} \Bigg[jF(\rho) \frac{e^{-jk\rho}}{2\pi\rho} \cdot \sum_{mn} P_{mn} e^{j\rho K_{mn}\cos(\theta_{mn}-\theta)} \\ \cdot \frac{K_{mn}\cos(\theta_{mn}-\theta)}{\sqrt{K_{mn}^2 - 2kK_{mn}\cos(\theta_{mn}-\theta)}} \Bigg] \end{aligned}$$

$$
\begin{aligned}
&\approx jF(\rho)\frac{e^{-jk\rho}}{2\pi\rho}\sum_{mn}P_{mn}e^{j\rho K_{mn}\cos(\theta_{mn}-\theta)} \\
&\quad\cdot\frac{K_{mn}\cos(\theta_{mn}-\theta)}{\sqrt{K_{mn}^2-2kK_{mn}\cos(\theta_{mn}-\theta)}} \\
&\quad\cdot j\left\{\left[K_{mn}\cos(\theta_{mn}-\theta)-k\right]\hat{\rho}+K_{mn}\sin(\theta_{mn}-\theta)\hat{\theta}\right\} \qquad (2.27)
\end{aligned}
$$

By using this result, (2.25) becomes

$$
\begin{aligned}
(E_{0n}^{+})_2 \approx\ & jkC_0\left\{\left[F(\rho)\frac{e^{-jk\rho}}{2\pi\rho}\sum_{mn}P_{mn}\right.\right. \\
&\cdot\frac{K_{mn}\cos(\theta_{mn}-\theta)}{\sqrt{K_{mn}^2-2kK_{mn}\cos(\theta_{mn}-\theta)}} \\
&\cdot\nabla_{xy}(\xi)\cdot\left\{\left[K_{mn}\cos(\theta_{mn}-\theta)-k\right]\hat{\rho}\right. \\
&\left.+K_{mn}\sin(\theta_{mn}-\theta)\hat{\theta}\right\} \\
&\left.\cdot e^{j\rho K_{mn}\cos(\theta_{mn}-\theta)}\right\}\overset{xy}{*}F(\rho)\frac{e^{-jk\rho}}{2\pi\rho}\Bigg\} \qquad (2.28)
\end{aligned}
$$

Also, from (2.26)

$$
\begin{aligned}
\nabla_{xy}(\xi) \approx\ & j\sum_{pq}P_{pq}K_{pq}\left[\cos(\theta_{pq}-\theta)\hat{\rho}+\sin(\theta_{pq}-\theta)\hat{\theta}\right] \\
&\cdot e^{j\rho K_{pq}\cos(\theta_{pq}-\theta)} \qquad (2.29)
\end{aligned}
$$

and

$$
\begin{aligned}
&\nabla_{xy}(\xi)\cdot\left\{\left[K_{mn}\cos(\theta_{mn}-\theta)-k\right]\hat{\rho}+K_{mn}\sin(\theta_{mn}-\theta)\hat{\theta}\right\} \\
=\ & j\sum_{pq}P_{pq}K_{pq}\left\{K_{mn}\left[\cos(\theta_{mn}-\theta)\cos(\theta_{pq}-\theta)\right.\right. \\
&\left.\left.+\sin(\theta_{mn}-\theta)\sin(\theta_{pq}-\theta)\right]-k\cos(\theta_{pq}-\theta)\right\}\cdot e^{j\rho K_{pq}\cos(\theta_{pq}-\theta)} \\
=\ & j\sum_{pq}P_{pq}\left[K_{pq}K_{mn}\cos(\theta_{mn}-\theta_{pq})-kK_{pq}\cos(\theta_{pq}-\theta)\right]
\end{aligned}
$$

$$\cdot e^{j\rho K_{pq}\cos(\theta_{pq}-\theta)}$$

$$= j\sum_{pq}\left(\vec{K}_{pq}\cdot\vec{K}_{mn}-k\hat{\rho}\cdot\vec{K}_{pq}\right]e^{j\rho K_{pq}\cos(\theta_{pq}-\theta)} \tag{2.30}$$

If this last expression is used in (2.28), it results

$$(E_{0n}^{+})_2 \approx -kC_0\left\{\left\{F(\rho)\frac{e^{-jk\rho}}{2\pi\rho}\sum_{mn}\sum_{pq}P_{mn}P_{pq}e^{j\rho K_{rs}\cos(\theta_{rs}-\theta)}\right.\right.$$
$$\left.\left.\cdot\frac{(\vec{K}_{mn}\cdot\hat{\rho})[\vec{K}_{pq}\cdot(\vec{K}_{mn}-k\hat{\rho})]}{\sqrt{\vec{K}_{mn}\cdot(\vec{K}_{mn}-2k\hat{\rho})}}\right\}\overset{xy}{*}F(\rho)\frac{e^{-jk\rho}}{2\pi\rho}\right\} \tag{2.31}$$

where, $\vec{K}_{rs}=\vec{K}_{mn}+\vec{K}_{pq}$.

Referring to Figure 2.2, equation (2.31) may be written in integral form as

$$(E_{0n}^{+})_2 \approx \frac{-kC_0}{(2\pi)^2}\sum_{mn}\sum_{pq}P_{mn}P_{pq}$$
$$\cdot\int_{x_2}\int_{y_2}\frac{(\vec{K}_{mn}\cdot\hat{\rho}_2)[\vec{K}_{pq}\cdot(\vec{K}_{mn}-k\hat{\rho}_2)]}{\sqrt{\vec{K}_{mn}\cdot(\vec{K}_{mn}-2k\hat{\rho}_2)}}F(\rho_2)F(\rho_{20})$$
$$\cdot\frac{e^{j\rho_2[K_{rs}\cos(\theta_{rs}-\theta_2)-k]-jk\rho_{20}}}{\rho_2\rho_{20}}dx_2dy_2 \tag{2.32}$$

Equation (2.32) may now be treated via a second stationary phase process [71]. As before, the stationary phase integration is accomplished via an elliptic coordinate (μ,δ) transformation similar to that described in Section 2.1. That is (1) rotation of the axes by θ, i.e.,

$$x_2 = x_2'\cos\theta-y_2'\sin\theta$$
$$y_2 = x_2'\sin\theta+y_2'\cos\theta \tag{2.33}$$

(2) shift of the origin in the $(x_2^{'}, y_2^{'})$ plane to a position halfway along ρ,

$$\begin{aligned} x_2^{''} &= x_2^{'} - \frac{\rho}{2} \\ y_2^{''} &= y_2^{'} \end{aligned} \tag{2.34}$$

then

$$\begin{aligned} x_2 &= \left(x_2^{''} + \frac{\rho}{2}\right)\cos\theta - y_2^{''}\sin\theta \\ y_2 &= \left(x_2^{''} + \frac{\rho}{2}\right)\sin\theta + y_2^{''}\cos\theta \end{aligned} \tag{2.35}$$

(3) conversion to elliptic coordinates,

$$\begin{aligned} x_2^{''} &= \frac{\rho}{2}\cosh\mu\cos\delta \\ y_2^{''} &= \frac{\rho}{2}\sinh\mu\sin\delta \end{aligned} \tag{2.36}$$

This results in

$$\begin{aligned} x_2 &= \frac{\rho}{2}[(1+\cosh\mu\cos\delta)\cos\theta - \sinh\mu\sin\delta\sin\theta] \\ y_2 &= \frac{\rho}{2}[(1+\cosh\mu\cos\delta)\sin\theta + \sinh\mu\sin\delta\cos\theta] \end{aligned} \tag{2.37}$$

$$\begin{aligned} \rho_2 &= \frac{\rho}{2}(\cosh\mu + \cos\delta) \\ \rho_{20} &= \frac{\rho}{2}(\cosh\mu - \cos\delta) \end{aligned} \tag{2.38}$$

$$\theta_2 = \tan^{-1}\left(\frac{y_2}{x_2}\right)$$

$$= \tan^{-1}\left[\frac{(1+\cosh\mu\cos\delta)\sin\theta+\sinh\mu\sin\delta\cos\theta}{(1+\cosh\mu\cos\delta)\cos\theta-\sinh\mu\sin\delta\sin\theta}\right] \tag{2.39}$$

By using the above transformation, equation (2.32) becomes

$$\begin{aligned}(E_{0n}^{+})_2 \approx\ & \frac{-kC_0}{(2\pi)^2}\sum_{mn}\sum_{pq}P_{mn}P_{pq} \\ & \cdot e^{j\frac{\rho K_{rs}}{2}\cos(\theta_{rs}-\theta)}\int_0^{\infty}e^{-j\rho k\cosh\mu} \\ & \cdot\left(\int_0^{2\pi}\frac{(\vec{K}_{mn}\cdot\hat{\rho}_2)[\vec{K}_{pq}\cdot(\vec{K}_{mn}-k\hat{\rho}_2)]}{\sqrt{\vec{K}_{mn}\cdot(\vec{K}_{mn}-2k\hat{\rho}_2)}}F(\rho_2)F(\rho_{20})\right. \\ & \left.\cdot e^{j\frac{\rho K_{rs}}{2}[\cosh\mu\cos\delta\cos(\theta_{rs}-\theta)+\sinh\mu\sin\delta\sin(\theta_{rs}-\theta)]}d\delta\right)d\mu\end{aligned} \tag{2.40}$$

whence we write for the δ integral

$$\begin{aligned}I_\delta =\ & \int_0^{2\pi}\frac{(\vec{K}_{mn}\cdot\hat{\rho}_2)[\vec{K}_{pq}\cdot(\vec{K}_{mn}-k\hat{\rho}_2)]}{\sqrt{\vec{K}_{mn}\cdot(\vec{K}_{mn}-2k\hat{\rho}_2)}}F(\rho_2)F(\rho_{20}) \\ & \cdot e^{j\frac{\rho K_{rs}}{2}[\cosh\mu\cos\delta\cos(\theta_{rs}-\theta)+\sinh\mu\sin\delta\sin(\theta_{rs}-\theta)]}d\delta\end{aligned} \tag{2.41}$$

It can be readily shown that using stationary phase integration in (2.41) yields

$$\begin{aligned}I_\delta \approx\ & \sqrt{2\pi}\frac{(\vec{K}_{mn}\cdot\hat{\rho}_2)[\vec{K}_{pq}\cdot(\vec{K}_{mn}-k\hat{\rho}_2)]}{\sqrt{\vec{K}_{mn}\cdot(\vec{K}_{mn}-2k\hat{\rho}_2)}}F(\rho_2)F(\rho_{20}) \\ & \cdot e^{j\frac{\rho K_{rs}}{2}[\cosh\mu\cos\delta\cos(\theta_{rs}-\theta)+\sinh\mu\sin\delta\sin(\theta_{rs}-\theta)]} \\ & \cdot\left(\frac{1}{j\frac{\rho K_{rs}}{2}[\cosh\mu\cos\delta\cos(\theta_{rs}-\theta)+\sinh\mu\sin\delta\sin(\theta_{rs}-\theta)]}\right)^{\frac{1}{2}}\end{aligned} \tag{2.42}$$

where a stationary phase condition on δ is given by

$$\tanh\delta = \tanh\mu\tan(\theta_{rs}-\theta) \tag{2.43}$$

Gill and Walsh [54], [55] have shown that at the stationary scatter point the surface wave vector $\vec{K}_{rs}$ is normal to the scattering ellipse (see Figure 2.3), and the angle between the transmitter and receiver as viewed from the scatter point is bisected by the ellipse normal at that point. Each portion of this bisection is seen in Figure 2.3 as bistatic angle ϕ. Based on these results, equation (2.42) becomes

$$\begin{aligned} I_\delta &\approx \sqrt{2\pi}\frac{(\vec{K}_{mn}\cdot\hat{\rho}_2)[\vec{K}_{pq}\cdot(\vec{K}_{mn}-k\hat{\rho}_2)]}{\sqrt{\vec{K}_{mn}\cdot(\vec{K}_{mn}-2k\hat{\rho}_2)}}\left(\frac{1}{\pm\sqrt{\cos\phi}}\right)\frac{F(\rho_2)F(\rho_{20})}{\sqrt{K_{rs}\rho_{s21}}} \\ &\quad \cdot e^{\pm j\rho_{s21}K_{rs}\cos\phi}e^{\mp\pi/4} \end{aligned} \tag{2.44}$$

where

$$\rho_{s21} = \frac{\rho_2+\rho_{20}}{2} = \frac{\rho}{2}\cosh\mu \tag{2.45}$$

Inserting (2.44)–(2.45) into (2.40), and rewrite this μ integral in terms of ρ_{s21}, equation (2.40) becomes

$$\begin{aligned} (E_{0n}^{+})_2 &\approx \frac{-kC_0}{(2\pi)^{3/2}}\sum_{mn}\sum_{pq}P_{mn}P_{pq}\cdot e^{j\frac{\vec{\rho}}{2}\cdot\vec{K}_{rs}} \\ &\quad \cdot\int_{\frac{\rho}{2}}^{\infty} e^{-j2\rho_{s21}k}\frac{(\vec{K}_{mn}\cdot\hat{\rho}_2)[\vec{K}_{pq}\cdot(\vec{K}_{mn}-k\hat{\rho}_2)]}{\sqrt{\vec{K}_{mn}\cdot(\vec{K}_{mn}-2k\hat{\rho}_2)}}\frac{1}{\pm\sqrt{K_{rs}\cos\phi}} \\ &\quad \cdot\frac{F(\rho_2)F(\rho_{20})}{\sqrt{\rho_{s21}[\rho_{s21}^2-(\frac{\rho}{2})^2]}}\cdot e^{\pm j\rho_{s21}K_{rs}\cos\phi}e^{\mp\pi/4}d\rho_{s21} \end{aligned} \tag{2.46}$$

This is the Fourier transformation result of the second-order normal electric field scattered from a time-invariant surface.

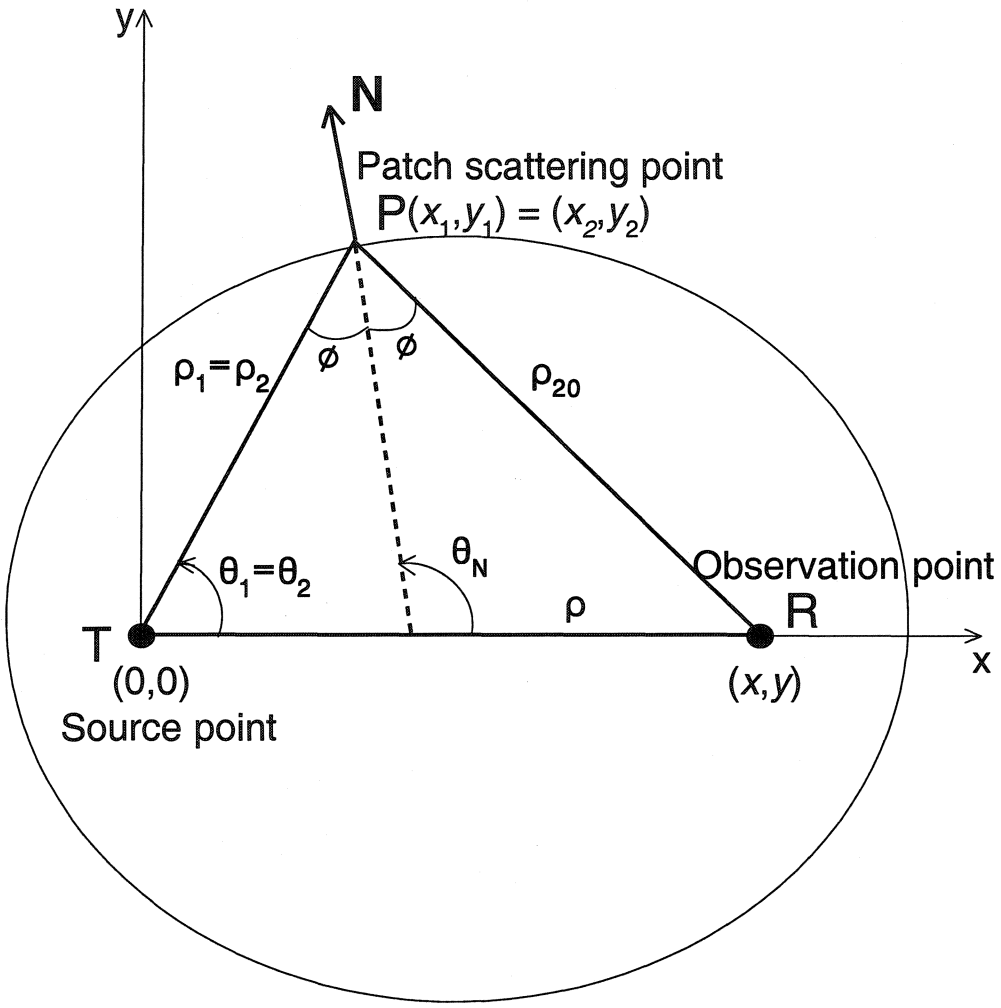

Figure 2.3: Depiction of the geometry associated with the second-order stationary phase condition. R and T are receiver and transmitter, respectively.

2.3 Application to Pulse Radar

Inverse Fourier transformation of equation (2.46) with respect to time t gives

$$
\begin{aligned}
(E_{0n}^{+})_2(t) \approx & \frac{-1}{(2\pi)^{3/2}}\Big[\mathcal{F}_t^{-1}(kC_0) \\
& * \sum_{mn}\sum_{pq} P_{mn}P_{pq}\cdot e^{j\frac{\vec{\rho}}{2}\cdot\vec{K}_{rs}} \\
& \cdot \int_{\frac{\rho}{2}}^{\infty} \delta(t-\frac{2\rho_{s21}}{c})\frac{(\vec{K}_{mn}\cdot\hat{\rho}_2)[\vec{K}_{pq}\cdot(\vec{K}_{mn}-K_0\hat{\rho}_2)]}{\sqrt{\vec{K}_{mn}\cdot(\vec{K}_{mn}-2K_0\hat{\rho}_2)}}\frac{1}{\pm\sqrt{K_{rs}\cos\phi}} \\
& \cdot \frac{F(\rho_2,\omega_0)F(\rho_{20},\omega_0)}{\sqrt{\rho_{s21}[\rho_{s21}^2-(\frac{\rho}{2})^2]}}\cdot e^{\pm j\rho_{s21}K_{rs}\cos\phi}e^{\mp\pi/4}d\rho_{s21}\Big]
\end{aligned}
\tag{2.47}
$$

where $*$ denotes time convolution, and ω_0 is the central angular frequency of a pulsed sinusoid. The $\delta()$ is the Dirac delta function and it has been assumed that

$$
\mathcal{F}_t^{-1}[F(\rho_2,\omega)F(\rho_{20},\omega)e^{-j2\rho_{s21}k}] \approx F(\rho_2,\omega_0)F(\rho_{20},\omega_0)\delta(t-\frac{2\rho_{s21}}{c}) \tag{2.48}
$$

where the attenuation functions, F, are a function of frequency ω. In the HF band, for any desirable pulse length of current, the variation of F corresponding to the variation in ω is small [53]. Thus, the inverse Fourier transform approximation in (2.48) is valid.

In general, the bistatic scatter analysis is not restricted to a particular type of source radiation, but here a dipole source is assumed. It is a well-known result that for the dipole source of length $\Delta\ell$

$$
kC_0 = -j\frac{\eta_0\Delta\ell}{c^2}\omega^2 I(\omega) \tag{2.49}
$$

where the source current $I(\omega)$ has a radian frequency ω. The constants c and

η_0 are the free space values of the speed of light and the intrinsic impedence, respectively. Therefore,

$$\mathcal{F}_t^{-1}(kC_0) = j\frac{\eta_0 \Delta\ell}{c^2}\frac{\partial^2}{\partial t^2}[i(t)] \tag{2.50}$$

where $i(t)$ is the dipole current in the time domain. As explained below, equation (2.50) is useful in modeling a wide range of transmitted signals, e.g., Frequency Modulated Continuous Wave (FMCW), pulsed sinusoids and so on. In particular, for a pulse radar system, the antenna current may be modeled as,

$$i(t) = I_0 e^{j\omega_0 t}[h(t) - h(t-\tau_0)] \tag{2.51}$$

where $h()$ is the Heaviside function and τ_0 is the pulse duration. Although this current is complex it may be realized physically by "in phase" and "quadrature" components. Also, real trigonometric sines and cosines are given by linear combinations of (2.51). Since the response equations are linear, superposition applies and thus any signal form may be generated.

From equation (2.51) it may be easily deduced that

$$\frac{\partial^2}{\partial t^2}[i(t)] = -{\omega_0}^2 I_0 e^{j\omega_0 t}[h(t) - h(t-\tau_0)] \tag{2.52}$$

where the leading and trailing edge impulse terms have been ignored for practical sampling purposes. Therefore, for the pulse system, (2.50) becomes

$$\mathcal{F}_t^{-1}(kC_0) = -j\eta_0 \Delta\ell I_0 {K_0}^2 e^{j\omega_0 t}[h(t) - h(t-\tau_0)] \tag{2.53}$$

where $K_0 = \omega_0/c$.

Now,

$$\begin{aligned} & e^{j\omega_0 t}[h(t) - h(t-\tau_0)] \overset{t}{*} \delta(t - \tfrac{2\rho_{s21}}{c}) \\ = \; & e^{j\omega_0(t-\frac{2\rho_{s21}}{c})}[h(t - \tfrac{2\rho_{s21}}{c}) - h(t - \tfrac{2\rho_{s21}}{c} - \tau_0)] \end{aligned} \tag{2.54}$$

Thus, (2.47) becomes

$$\begin{aligned} (E_{0n}^{+})_2(t) \approx & \frac{j\eta_0 \Delta\ell I_0 K_0^2}{(2\pi)^{3/2}} \sum_{mn}\sum_{pq} P_{mn}P_{pq} \cdot e^{j\frac{\vec{\rho}}{2}\cdot\vec{K}_{rs}} e^{j\omega_0 t} \\ & \int_{\frac{c(t-\tau_0)}{2}}^{\frac{ct}{2}} \frac{(\vec{K}_{mn}\cdot\hat{\rho}_2)[\vec{K}_{pq}\cdot(\vec{K}_{mn} - K_0\hat{\rho}_2)]}{\sqrt{\vec{K}_{mn}\cdot(\vec{K}_{mn} - 2K_0\hat{\rho}_2)}} \frac{1}{\pm\sqrt{K_{rs}\cos\phi}} \\ & \frac{F(\rho_2,\omega_0)F(\rho_{20},\omega_0)}{\sqrt{\rho_{s21}[\rho_{s21}^2 - (\frac{\rho}{2})^2]}} \cdot e^{j\rho_{s21}(\pm K_{rs}\cos\phi - 2K_0)} e^{j\mp\pi/4} d\rho_{s21} \end{aligned} \tag{2.55}$$

Defining

$$\begin{aligned} \rho_{os21} &= \frac{\frac{ct}{2} + \frac{c(t-\tau_0)}{2}}{2} = \frac{c(t-\tau_0/2)}{2} \\ \Delta\rho_{s21} &= \frac{c\tau_0}{2} \end{aligned} \tag{2.56}$$

gives

$$\begin{aligned} \rho_{os21} - \Delta\rho_{s21}/2 &= \frac{c(t-\tau_0)}{2} \\ \rho_{os21} + \Delta\rho_{s21}/2 &= \frac{ct}{2} \end{aligned} \tag{2.57}$$

so that (2.55) may be written as,

$$(E_{0n}^{+})_2(t) \approx \frac{-j\eta_0 \Delta\ell I_0 K_0^2}{(2\pi)^{3/2}} \sum_{mn}\sum_{pq} P_{mn}P_{pq} \cdot e^{j\frac{\vec{\rho}}{2}\cdot\vec{K}_{rs}} e^{j\omega_0 t} e^{j\mp\pi/4}$$

$$\int_{\rho_{os21}-\Delta\rho_{s21}/2}^{\rho_{os21}+\Delta\rho_{s21}/2} \frac{(\vec{K}_{mn}\cdot\hat{\rho}_2)[\vec{K}_{pq}\cdot(\vec{K}_{mn}-K_0\hat{\rho}_2)]}{\sqrt{\vec{K}_{mn}\cdot(\vec{K}_{mn}-2K_0\hat{\rho}_2)}} \frac{1}{\pm\sqrt{K_{rs}\cos\phi}}$$
$$\frac{F(\rho_2,\omega_0)F(\rho_{20},\omega_0)}{\sqrt{\rho_{s21}[\rho_{s21}^2-(\frac{\rho}{2})^2]}}\cdot e^{j\rho_{s21}(\pm K_{rs}\cos\phi-2K_0)}d\rho_{s21} \tag{2.58}$$

As for the elliptical analysis in [50], the phase term in (2.58) maybe written as

$$\begin{aligned}&\rho_{s21}(\pm K_{rs}\cos\phi-2K_0)\\ =\;&\rho_{os21}(\pm K_{rs}\cos\phi_0-2K_0)+\left(\pm\tfrac{K_{rs}}{\cos\phi_0}-2K_0\right)\rho_{s21}'\end{aligned} \tag{2.59}$$

where $\rho_{s21}' = \rho_{s21} - \rho_{os21}$ and

$$\cos\phi_0 = \sqrt{1-\left(\frac{\rho/2}{\rho_{os21}}\right)^2\sin^2\theta_N} \tag{2.60}$$

where θ_N is the scatter ellipse normal direction.

Equation (2.59) is valid only for $\rho_{os21} >> \rho_{s21}'$. By using (2.59) in (2.58) and invoking a "slowly varying" assumption on all but the exponential term there results,

$$\begin{aligned}(E_{0n}^{+})_2(t) \;\approx\;& \frac{-j\eta_0\Delta\ell I_0K_0^2}{(2\pi)^{3/2}}\sum_{mn}\sum_{pq}P_{mn}P_{pq}\cdot e^{j\frac{\vec{\rho}}{2}\cdot\vec{K}_{rs}}e^{j\omega_0 t}e^{\mp j\pi/4}(\pm\sqrt{K_{rs}\cos\phi_0})\\ &\cdot\frac{(\vec{K}_{mn}\cdot\hat{\rho}_2)[\vec{K}_{pq}\cdot(\vec{K}_{mn}-K_0\hat{\rho}_2)]}{K_{rs}\cos\phi_0\sqrt{\vec{K}_{mn}\cdot(\vec{K}_{mn}-2K_0\hat{\rho}_2)}}\frac{F(\rho_{02},\omega_0)F(\rho_{020},\omega_0)}{\sqrt{\rho_{os21}[\rho_{os21}^2-(\frac{\rho}{2})^2]}}\\ &\cdot e^{j\rho_{os21}(\pm K_{rs}\cos\phi_0-2K_0)}\int_{-\Delta\rho_{s21}/2}^{\Delta\rho_{s21}/2}e^{j(\pm K_{rs}\cos\phi_0-2K_0)\rho_{s21}'}d\rho_{s21}'\end{aligned} \tag{2.61}$$

where $\dfrac{\rho_{02}+\rho_{020}}{2} = \rho_{os21}$ is centered between $c(t-\tau_0)/2$ and $ct/2$. The fact that ρ_2, ρ_{20}, and ϕ vary only slightly over the "patch" has been indicated by writing their representative values as ρ_{02}, ρ_{020}, and ϕ_0, respectively.

Using (2.56),

$$e^{j\omega_0 t}e^{-j2\rho_{os21}K_0} = e^{jK_0ct}e^{-j2\frac{c(t-\tau_0/2)}{2}K_0} = e^{jK_0c\tau_0/2} = e^{jK_0\Delta\rho_{s21}} \tag{2.62}$$

Inserting (2.62) into (2.61) gives

$$\begin{aligned}(E_{0n}^{+})_2(t) \approx\ & \frac{-j\eta_0\Delta\ell I_0K_0^2}{(2\pi)^{3/2}}\sum_{mn}\sum_{pq}P_{mn}P_{pq}\cdot e^{j\frac{\vec{\rho}}{2}\cdot\vec{K}_{rs}}e^{jK_0\Delta\rho_{s21}}e^{\mp j\pi/4} \\ & \cdot(\pm\sqrt{K_{rs}\cos\phi_0})\frac{(\vec{K}_{mn}\cdot\hat{\rho}_2)[\vec{K}_{pq}\cdot(\vec{K}_{mn}-K_0\hat{\rho}_2)]}{K_{rs}\cos\phi_0\sqrt{\vec{K}_{mn}\cdot(\vec{K}_{mn}-2K_0\hat{\rho}_2)}} \\ & \cdot\frac{F(\rho_{02},\omega_0)F(\rho_{020},\omega_0)}{\sqrt{\rho_{os21}[\rho_{os21}^2-(\frac{\rho}{2})^2]}}e^{\pm j\rho_{s021}K_{rs}\cos\phi_0} \\ & \cdot\int_{-\Delta\rho_{s21}/2}^{\Delta\rho_{s21}/2}e^{j(\pm K_{rs}\cos\phi_0-2K_0)\rho_{s21}'}d\rho_{s21}'\end{aligned} \tag{2.63}$$

Now, setting the electromagnetic coupling coefficient Γ_{EP}

$$\Gamma_{EP} = \frac{-(\vec{K}_{mn}\cdot\hat{\rho}_2)[\vec{K}_{pq}\cdot(\vec{K}_{mn}-K_0\hat{\rho}_2)]}{K_{rs}\cos\phi_0\sqrt{\vec{K}_{mn}\cdot(\vec{K}_{mn}-2K_0\hat{\rho}_2)}} \tag{2.64}$$

gives

$$\begin{aligned}(E_{0n}^{+})_2(t) \approx\ & \frac{-j\eta_0\Delta\ell I_0K_0^2}{(2\pi)^{3/2}}\sum_{mn}\sum_{pq}P_{mn}P_{pq}\cdot e^{j\frac{\vec{\rho}}{2}\cdot\vec{K}_{rs}}e^{jK_0\Delta\rho_{s21}}e^{\mp j\pi/4} \\ & \cdot\Gamma_{EP}(\pm\sqrt{K_{rs}\cos\phi_0}) \\ & \cdot\frac{F(\rho_{02},\omega_0)F(\rho_{020},\omega_0)}{\sqrt{\rho_{os21}[\rho_{os21}^2-(\frac{\rho}{2})^2]}}e^{\pm j\rho_{s021}K_{rs}\cos\phi_0} \\ & \cdot\int_{-\Delta\rho_{s21}/2}^{\Delta\rho_{s21}/2}e^{j(\pm K_{rs}\cos\phi_0-2K_0)\rho_{s21}'}d\rho_{s21}'\end{aligned} \tag{2.65}$$

Using

$$\begin{aligned}
&\int_{-\Omega}^{\Omega} e^{jxt}dx \\
&= \frac{2\sin(\Omega t)}{t} \\
&= 2\Omega\frac{\sin(\Omega t)}{\Omega t} \\
&= 2\Omega Sa(\Omega t)
\end{aligned} \tag{2.66}$$

in evaluating the integral in (2.63), the time-dependent E-field becomes

$$\begin{aligned}
(E_{0n}^{+})_2(t) \approx\ & \frac{-j\eta_0\Delta\ell I_0 K_0^2}{(2\pi)^{3/2}}\sum_{mn}\sum_{pq} P_{mn}P_{pq}\cdot e^{j\frac{\vec{\rho}}{2}\cdot\vec{K}_{rs}}e^{jK_0\Delta\rho_{s21}}e^{-j\pi/4} \\
&\cdot\Gamma_{EP}(\pm\sqrt{K_{rs}\cos\phi_0})\frac{F(\rho_{02},\omega_0)F(\rho_{020},\omega_0)}{\sqrt{\rho_{s021}[\rho_{s021}^2-(\frac{\rho}{2})^2]}} \\
&\cdot e^{j\rho_{s021}K_{rs}\cos\phi_0}\Delta\rho_{s21}Sa\left[\frac{\Delta\rho_{s21}}{2}\left(\frac{\pm K_{rs}}{\cos\phi_0}-2K_0\right)\right]
\end{aligned} \tag{2.67}$$

It should be noted that the second $Sa(\cdot)$ resulting from

$$e^{j(-K_{rs}\cos\phi_0-2K_0)\rho'_{s21}} \tag{2.68}$$

may be discarded as small, so the second-order E-field for patch scatter is

$$\begin{aligned}
(E_{0n}^{+})_2(t) \approx\ & \frac{-j\eta_0\Delta\ell I_0 K_0^2}{(2\pi)^{3/2}}\sum_{mn}\sum_{pq} P_{mn}P_{pq}\cdot e^{j\frac{\vec{\rho}}{2}\cdot\vec{K}_{rs}}e^{jK_0\Delta\rho_{s21}}e^{-j\pi/4} \\
&\cdot\Gamma_{EP}\sqrt{K_{rs}\cos\phi_0}\frac{F(\rho_{02},\omega_0)F(\rho_{020},\omega_0)}{\sqrt{\rho_{s021}[\rho_{s021}^2-(\frac{\rho}{2})^2]}} \\
&\cdot e^{j\rho_{s021}K_{rs}\cos\phi_0}\Delta\rho_{s21}Sa\left[\frac{\Delta\rho_{s21}}{2}\left(\frac{K_{rs}}{\cos\phi_0}-2K_0\right)\right]
\end{aligned} \tag{2.69}$$

At this stage of the analysis, the time-dependant second-order normal E-field

for patch scatter from time-invariant surface has been derived.

Chapter 3

The Second-order Bistatic HF Radar Cross Section for "Patch Scatter" from the Ocean Surface

In the previous chapter, a general solution, in the context of bistatic HF radar, for electromagnetic time-invariant rough surface scatter has been presented. In this chapter, the results will be applied to develop a model for an ocean surface cross section. Unlike the time-invariant surface, the ocean surface is random and nonlinear. The randomness may be introduced into the model by treating the Fourier coefficients in the series representing the surface as random variables.

3.1 Ocean Surface Specifications

The time-varying nature of the ocean surface may be included in equations (2.3) and (2.26) by treating sea surfaces as three-dimensional periodic surfaces in both

space (x, y) and time (t). Then the ocean surface ξ may be represented as

$$\xi(x,y,t) = \sum_{\vec{K},\omega} P_{\vec{K},\omega} e^{j\vec{\rho}\cdot\vec{K}+j\omega t} \tag{3.1}$$

The coefficients P_{mn} in (2.3) and P_{pq} in (2.26) are replaced by

$$\sum_{\omega_1} P_{mn,\omega_1} e^{j\omega_1 t} \text{ and } \sum_{\omega_2} P_{pq,\omega_2} e^{j\omega_2 t} \tag{3.2}$$

respectively. The corresponding expression of (2.69) is then given by

$$\begin{aligned}(E_{0n}^{+})_2(t) \approx\ & \frac{-j\eta_0 \Delta\ell I_0 K_0^2 \Delta\rho_{s21} e^{-j\pi/4} e^{jK_0\Delta\rho_{s21}}}{(2\pi)^{3/2}} \\ & \sum_{\omega_1} P_{mn,\omega_1} e^{j\omega_1 t} \sum_{\omega_2} P_{pq,\omega_2} e^{j\omega_2 t} e^{j\frac{\vec{\rho}}{2}\cdot\vec{K}_{rs}} \\ & \cdot\Gamma_{EP}\sqrt{K_{rs}\cos\phi_0}\frac{F(\rho_{02},\omega_0)F(\rho_{020},\omega_0)}{\sqrt{\rho_{os21}[\rho_{os21}^2-(\frac{\rho}{2})^2]}} \\ & \cdot e^{j\rho_{os21}K_{rs}\cos\phi_0} Sa\left[\frac{\Delta\rho_{s21}}{2}\left(\frac{K_{rs}}{\cos\phi_0}-2K_0\right)\right]\end{aligned} \tag{3.3}$$

Equation (3.3) is the field resulting from double scattering from two distinct first-order waves. It should be noted that the second-order field also arises from hydrodynamic coupling of first-order surface waves, and it has been given by Gill [53] as

$$\begin{aligned}(E_{0n}^{+})_2(t) \approx\ & \frac{-j\eta_0 \Delta\ell I_0 K_0^2 \Delta\rho_{s21} e^{-j\pi/4} e^{jK_0\Delta\rho_{s21}}}{(2\pi)^{3/2}} \\ & \sum_{\omega_1} P_{mn,\omega_1} e^{j\omega_1 t} \sum_{\omega_2} P_{pq,\omega_2} e^{j\omega_2 t} e^{j\frac{\vec{\rho}}{2}\cdot\vec{K}_{rs}} \\ & \cdot\Gamma_{H}\sqrt{K_{rs}\cos\phi_0}\frac{F(\rho_{02},\omega_0)F(\rho_{020},\omega_0)}{\sqrt{\rho_{os21}[\rho_{os21}^2-(\frac{\rho}{2})^2]}}\end{aligned}$$

$$\cdot e^{j\rho_{os21}K_{rs}\cos\phi_0} Sa\left[\frac{\Delta\rho_{s21}}{2}\left(\frac{K_{rs}}{\cos\phi_0} - 2K_0\right)\right] \tag{3.4}$$

where Γ_H is the hydrodynamic coupling coefficient. Comparing the second-order field arising because of the hydrodynamic coupling of first-order surface waves with (3.3), it is clear that the two second-order terms may be combined as

$$\begin{aligned}(E_{0n}^{+})_2(t) \approx\ & \frac{-j\eta_0\Delta\ell I_0 K_0^2 \Delta\rho_{s21} e^{-j\pi/4} e^{jK_0\Delta\rho_{s21}}}{(2\pi)^{3/2}} \\ & \cdot \sum_{\omega_1} P_{mn,\omega_1} e^{j\omega_1 t} \sum_{\omega_2} P_{pq,\omega_2} e^{j\omega_2 t} e^{j\frac{\vec{\rho}}{2}\cdot\vec{K}_{rs}} \\ & \cdot \Gamma_P \sqrt{K_{rs}\cos\phi_0} \frac{F(\rho_{02},\omega_0)F(\rho_{020},\omega_0)}{\sqrt{\rho_{os21}[\rho_{os21}^2 - (\frac{\rho}{2})^2]}} \\ & \cdot e^{j\rho_{os21}K_{rs}\cos\phi_0} Sa\left[\frac{\Delta\rho_{s21}}{2}\left(\frac{K_{rs}}{\cos\phi_0} - 2K_0\right)\right]\end{aligned} \tag{3.5}$$

where the whole coupling coefficient Γ_P includes the second-order electromagnetic Γ_{EP} and hydrodynamic Γ_H effects, thus

$$\Gamma_P = \Gamma_{EP} + \Gamma_H \tag{3.6}$$

The hydrodynamic coupling coefficient on identifying K as K_{rs} is given, for example, by Walsh *et al.* [69] for deep water as

$$\Gamma_H = \frac{1}{2}\left\{K_1 + K_2 + \frac{g}{w_1 w_2}(K_1K_2 - \vec{K}_1\cdot\vec{K}_2)\left[\frac{gK + (w_1+w_2)^2}{gK - (w_1+w_2)^2}\right]\right\} \tag{3.7}$$

where ω_1, ω_2 are angular frequencies of the first- and second ocean waves.

As the ocean surface can be assumed statistically stationary within a time frame of several minutes, it follows that the electric field $E(t)$ will be stationary as well. An auto-correlation function, with respect to t, for the electric field at the

receiving antenna may be defined as,

$$R(\tau) = \frac{A_r}{2\eta_0} < E(t+\tau), E^*(t) > \tag{3.8}$$

where $*$ represents the complex conjugation, and $<>$ denotes the statistical or ensemble average. The effective free space area A_r, as may be found in any antenna text, is given by

$$A_r = \frac{\lambda_0^2}{4\pi} G_r \tag{3.9}$$

where λ_0 is the free space wavelength and G_r is the free space gain of the receiving antenna.

With the assumptions of statistical stationarity for the surface and the statistical independence of the Fourier coefficients, we may define the power spectrum of the ocean surface due to first-order waves as [72]

$$< P^*_{\vec{K},\omega}, P_{\vec{K'},\omega'} >= \begin{cases} N^2 W S(\vec{K},\omega) & \text{if } \vec{K} = \vec{K'}, \omega = \omega' \\ 0 & \text{otherwise} \end{cases} \tag{3.10}$$

where N is the fundamental wavenumber and W the fundamental frequency of the surface. The function $S(\vec{K},\omega)$ is a three-dimensional power density spectrum of the ocean surface for linear or "first-order" ocean waves. It has been shown by

Gill [53] that

$$< P^{*}_{\vec{K}_1,\omega_1}, P_{\vec{K}_2',\omega_2'} >< P^{*}_{\vec{K}_1,\omega_1}, P_{\vec{K}_2',\omega_2'} >= \begin{cases} 2N_1^2 W_1 N_2^2 W_2 S(\vec{K}_1,\omega_1) S(\vec{K}_2,\omega_2) \\ (\text{if } \vec{K}_1 = \vec{K}_1', \omega_1 = \omega_1', \vec{K}_2 = \vec{K}_2', \omega_2 = \omega_2') \\ 0 \\ (\text{otherwise}) \end{cases} \tag{3.11}$$

If (3.5) and (3.11) are applied to (3.8), the auto-correlation function for the electric field becomes

$$\begin{aligned} R_{2P}(\tau) \;=\; & \frac{A_r}{2\eta_0} \frac{\eta_0^2 |\Delta\ell I_0|^2 K_0^4 (\Delta\rho_{s21})^2}{(2\pi)^3} \\ & \cdot 2N_1^2 W_1 \sum_{\omega_1} S(K_1,\omega_1) e^{j\omega_1\tau} N_2^2 W_2 \sum_{\omega_2} S(K_2,\omega_2) e^{j\omega_2\tau} \\ & \cdot |\Gamma_P|^2 K_{rs} \cos\phi_0 \frac{|F(\rho_{02},\omega_0) F(\rho_{020},\omega_0)|^2}{\rho_{os21}[\rho_{os21}^2 - (\frac{\rho}{2})^2]} \\ & \cdot Sa^2 \left[\frac{\Delta\rho_{s21}}{2} \left(\frac{K_{rs}}{\cos\phi_0} - 2K_0 \right) \right] \end{aligned} \tag{3.12}$$

The three-dimensional spectrum can be further reduced as [73]

$$S(\vec{K},\omega) = \frac{1}{2} \sum_{m=\pm 1} S(\vec{K}) \delta(\omega + m\sqrt{gK}) \tag{3.13}$$

Here $S(\vec{K})$ is a two-dimensional wave height spectrum. If we let the surface wavenumber N and the fundamental frequency W become very small and identify

$$N^2 \sim d^2\vec{K} \;\text{ and }\; W \sim d\omega, \tag{3.14}$$

equation (3.12) may be written as

$$
\begin{aligned}
R_{2P}(\tau) \;=\; & \frac{1}{4}\frac{A_r}{\eta_0}\frac{\eta_0^2|\Delta\ell I_0|^2 K_0^4(\Delta\rho_{s21})^2}{(2\pi)^3} \\
& \cdot \sum_{m_1=\pm 1}\int_{-\infty}^{\infty}\int_{-\infty}^{\infty} S(m_1\vec{K}_1)e^{j\omega_1\tau}\sum_{m_2=\pm 1}\int_{-\infty}^{\infty}\int_{-\infty}^{\infty} S(m_2\vec{K}_2)e^{j\omega_2\tau} \\
& \cdot|\Gamma_P|^2 K_{rs}\cos\phi_0\frac{|F(\rho_{02},\omega_0)F(\rho_{020},\omega_0)|^2}{\rho_{os21}[\rho_{os21}^2-(\frac{\rho}{2})^2]} \\
& \cdot Sa^2\left[\frac{\Delta\rho_{s21}}{2}\left(\frac{K_{rs}}{\cos\phi_0}-2K_0\right)\right] d^2\vec{K}_1 d^2\vec{K}_2
\end{aligned}
\tag{3.15}
$$

where the δ function in (3.13) has been used to evaluate the ω integral. Here, it is understood that

$$
\omega_1 = -m_1\sqrt{gK_1}\;\;,\;\;\omega_2 = -m_2\sqrt{gK_2} \tag{3.16}
$$

where $m_1, m_2 = \pm 1$ are indicators for Doppler frequency region for second-order cross section.

3.2 Derivation of the Second-order Bistatic HF Radar Cross Section for "Patch Scatter"

Noting that the integration variable $d^2\vec{K}$ of equation (3.15) may be written in polar coordinates as

$$
d^2\vec{K} = KdKd\theta_{\vec{K}} \tag{3.17}
$$

and that the Fourier transform has the property

$$
\mathcal{F}_t(e^{j\omega_0\tau}) = \delta(\omega-\omega_0), \tag{3.18}
$$

Fourier transform of (3.15) may now be taken to produce an average power spectrum of the ocean scatter signal $P_{2P}(\omega_d)$ from the patch. With (3.17)–(3.18) being applied to (3.15),

$$\begin{aligned} P_{2P}(\omega_d) &= \mathcal{F}_t[R_{2P}(\tau)] \\ &= \pi\frac{A_r}{2\eta_0}\frac{\eta_0^2|\Delta\ell I_0|^2K_0^4(\Delta\rho_{s21})^2}{(2\pi)^3} \\ &\quad \cdot\sum_{m_1=\pm1}\sum_{m_2=\pm1}\int_{-\pi}^{\pi}\int_{-\infty}^{\infty}\int_{-\pi}^{\pi}\int_{-\infty}^{\infty}S(m_1\vec{K}_1)S(m_2\vec{K}_2) \\ &\quad |\Gamma_P|^2K_{rs}\cos\phi_0\frac{|F(\rho_{02},\omega_0)F(\rho_{020},\omega_0)|^2}{\rho_{os21}[\rho_{os21}^2-(\frac{\rho}{2})^2]} \\ &\quad \cdot Sa^2\left[\frac{\Delta\rho_{s21}}{2}\left(\frac{K_{rs}}{\cos\phi_0}-2K_0\right)\right] \\ &\quad \cdot\delta(\omega_d+m_1\sqrt{gK_1}+m_2\sqrt{gK_2}) \\ &\quad \cdot K_1K_2dK_1d\theta_{\vec{K}_1}dK_2d\theta_{\vec{K}_2} \end{aligned} \tag{3.19}$$

where ω_d is Doppler frequency, and $P_{2P}(\omega_d)$ can also be referred as the radar Doppler spectrum.

Similar to the analysis in references [54] and [55], an expression for an elementary patch area dA of the scatter surface (see Figure 3.1) in terms of the bistatic scatter geometry may be approximated as

$$dA = \frac{(\rho_{02}\rho_{020})^2}{\rho_{os21}[\rho_{os21}^2-(\frac{\rho}{2})^2]}d\theta_N\Delta\rho_{s21} \tag{3.20}$$

Here θ_N is equal to the direction $\theta_{\vec{K_{rs}}}$. Referring to (3.19) and (3.20), it is noted that

$$\frac{dP_{2P}(\omega_d)}{dA} = \pi\frac{A_r}{2\eta_0}\frac{\eta_0^2|\Delta\ell|^2I_0^2K_0^4\Delta\rho_{s21}}{(2\pi)^3}$$

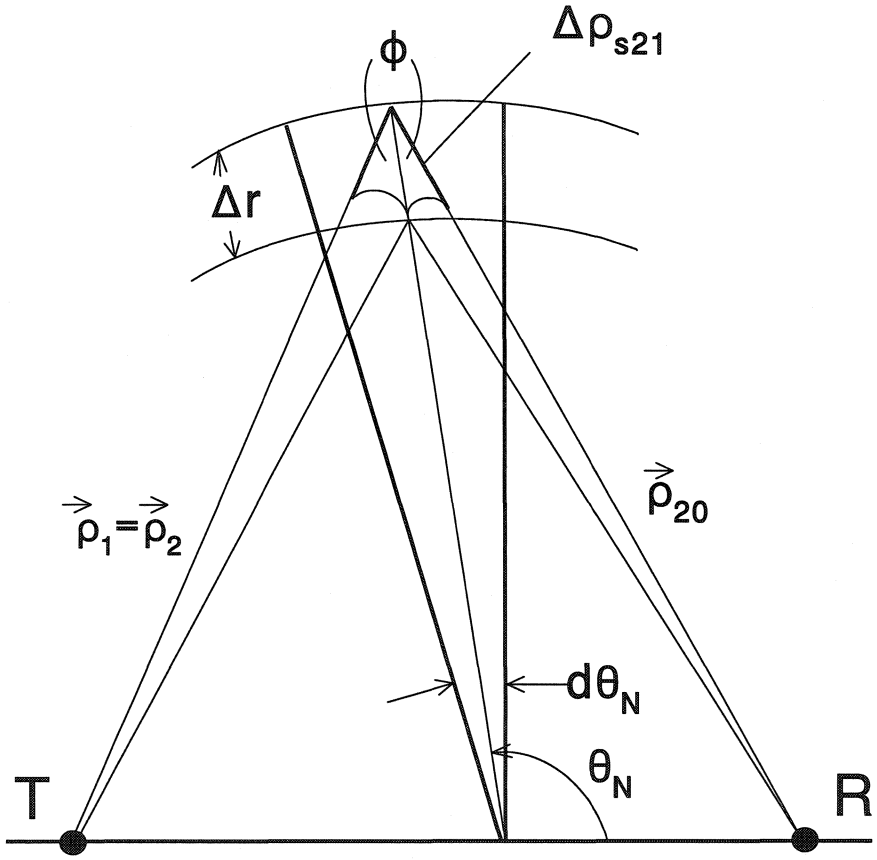

Figure 3.1: An expanded view showing an elemental scattering region. In the text the variables ρ_{02}, ρ_{020}, and ϕ_0 are used as representative values of ρ_2, ρ_{20}, and ϕ, respectively.

$$\cdot \sum_{m_1=\pm 1} \sum_{m_2=\pm 1} \int_{-\infty}^{\infty} \int_{-\pi}^{\pi} \int_{-\infty}^{\infty} S(m_1\vec{K}_1) S(m_2\vec{K}_2)$$
$$\cdot |\Gamma_P|^2 K_{rs}^2 \cos\phi_0 \frac{|F(\rho_{02},\omega_0)F(\rho_{020},\omega_0)|^2}{(\rho_{02}\rho_{020})^2}$$
$$\cdot Sa^2 \left[\frac{\Delta\rho_{s21}}{2}\left(\frac{K_{rs}}{\cos\phi_0} - 2K_0\right)\right] K_1$$
$$\cdot \delta(\omega_d + m_1\sqrt{gK_1} + m_2\sqrt{gK_2}) dK_1 d\theta_1 dK_{rs} \qquad (3.21)$$

in which the conversion of the K_2 integration to an integral over K_{rs} is accomplished via the stipulation that $\vec{K}_2 = \vec{K}_{rs} - \vec{K}_1$.

The bistatic radar range equation modified from the standard radar range equation (Appendix B) is

$$\frac{dP_{2P}(\omega_d)}{dA} = \frac{\lambda_0^2 P_t G_t G_r |F(\rho_{02},\omega_0)F(\rho_{020},\omega_0)|^2}{(4\pi)^3(\rho_{02}\rho_{020})^2} \sigma_{2P}(\omega_d) \qquad (3.22)$$

where $\sigma_{2P}(\omega_d)$ is the average radar cross section of the patch surface normalized to the area of the scattering patch. P_t and G_t are the transmitted power and free space gain of the transmitting antenna, respectively. For a vertical dipole source,

$$\begin{aligned} P_t G_t &= \frac{\eta_0 |\Delta\ell| I_0^2 K_0^2}{8\pi} \\ G_r &= \frac{4\pi A_r}{\lambda_0^2} \end{aligned} \qquad (3.23)$$

Then, comparing (3.21) and (3.22), it is easy to see that the second-order bistatic "patch scatter" cross section must be given by

$$\begin{aligned} \sigma_{2P}(\omega_d) = {} & 2^3\pi K_0^2 \Delta\rho_{s21} \sum_{m_1=\pm 1} \sum_{m_2=\pm 1} \int_{-\infty}^{\infty} \int_{-\pi}^{\pi} \int_{-\infty}^{\infty} S(m_1\vec{K}_1) S(m_2\vec{K}_2) \\ & \cdot |\Gamma_P|^2 K_{rs}^2 \cos\phi_0 \cdot Sa^2 \left[\frac{\Delta\rho_{s21}}{2}\left(\frac{K_{rs}}{\cos\phi_0} - 2K_0\right)\right] K_1 \end{aligned}$$

$$\delta(\omega_d + m_1\sqrt{gK_1} + m_2\sqrt{gK_2})dK_1 d\theta_{\vec{K}_1} dK_{rs} \tag{3.24}$$

It is readily checked that (3.24) has the same form as the result derived by Gill [54], [55] except that the electromagnetic coupling coefficient as given explicitly in equation (2.64) is different. For comparison, Gill's result [53], [54] is

$$\begin{aligned}\Gamma_{EP} &= \left\{\frac{j\sqrt{\vec{K}_{mn}\cdot(\vec{K}_{mn}-2K_0\hat{\rho}_2)}+K_0}{K_0^2+\vec{K}_{mn}\cdot(\vec{K}_{mn}-2K_0\hat{\rho}_2)}\right\} \\ &\quad\cdot\left\{\frac{K_0(\vec{K}_{mn}\cdot\hat{\rho}_2)[\vec{K}_{pq}\cdot(\vec{K}_{mn}-K_0\hat{\rho}_2)]}{K_{rs}\cos\phi_0\sqrt{\vec{K}_{mn}\cdot(\vec{K}_{mn}-2K_0\hat{\rho}_2)}}\right\}\end{aligned} \tag{3.25}$$

As explained in Sections 1.3 and 2.1, this difference comes from the different order of carrying out the analysis associated with equation (2.1).

3.3 Verifications

In order to verify the important result in equation (3.24), two properties are considered: (1) the complete form of the bistatic HF radar patch-scatter cross section is shown to reduce to the proper monostatic models [69] when the appropriate geometry for backscatter is introduced; (2) the electromagnetic coupling coefficient for the bistatic case is seen to incorporate its monostatic counterpart as given in [69].

3.3.1 The Complete Equation Form

If, as in [74], the relationship

$$\lim_{M\to\infty} MSa^2(Mx) = \pi\delta(x) \tag{3.26}$$

is applied to (3.24), then

$$\begin{aligned} & \Delta\rho_{s21} Sa^2 \left[\tfrac{\Delta\rho_{s21}}{2}\left(\tfrac{K_{rs}}{\cos\phi_0} - 2K_0\right)\right] \\ = \; & 2\cos\phi_0 \tfrac{\Delta\rho_{s21}}{2\cos\phi_0} Sa^2 \left[\tfrac{\Delta\rho_{s21}}{2\cos\phi_0}\left(K_{rs} - 2K_0\cos\phi_0\right)\right] \\ = \; & 2\pi\cos\phi_0 \delta\left(K_{rs} - 2K_0\cos\phi_0\right) \end{aligned} \tag{3.27}$$

where $\Delta\rho_{s21} \to \infty$ is assumed. Further, inserting this into (3.24) and considering the property of the Dirac delta function gives

$$\begin{aligned} \sigma_{2P}(\omega_d) = \; & 2^6\pi^2 K_0^4 \cos^4\phi_0 \sum_{m_1=\pm1}\sum_{m_2=\pm1}\int_{-\pi}^{\pi}\int_{-\infty}^{\infty} S(m_1\vec{K}_1)S(m_2\vec{K}_2) \\ & \cdot|\Gamma_P|^2 K_1 \delta(\omega_d + m_1\sqrt{gK_1} + m_2\sqrt{gK_2}) dK_1 d\theta_{\vec{K}_1} \end{aligned} \tag{3.28}$$

For backscattering, $\phi_0 = 0$ and (3.28) simplifies to

$$\begin{aligned} \sigma_{2P}(\omega_d) = \; & 2^6\pi^2 K_0^4 \sum_{m_1=\pm1}\sum_{m_2=\pm1}\int_{-\pi}^{\pi}\int_{-\infty}^{\infty} S(m_1\vec{K}_1)S(m_2\vec{K}_2) \\ & \cdot|\Gamma_P|^2 K_1 \delta(\omega_d + m_1\sqrt{gK_1} + m_2\sqrt{gK_2}) dK_1 d\theta_{\vec{K}_1} \end{aligned} \tag{3.29}$$

Here, (3.29) is similar in form to Barrick's second-order cross section which is based on perturbation theory [6], and it is exactly the same as that of Walsh *et al.* [69] whose model has been used extensively in HF radar applications on the Eastern Canada Coast (e.g., [33]–[36], [38]).

3.3.2 The Electromagnetic Coupling Coefficient

While the deep-water hydrodynamic coupling coefficient appears in all similar analyses (see, for example, [75]), the electromagnetic factor differs. As a result of

the analysis in the previous sections, the electromagnetic coupling coefficient for bistatic scatter in equations (3.24) and (3.28) is given in (2.64) as

$$\Gamma_{EP} = \frac{-(\vec{K}_{mn} \cdot \hat{\rho}_2)[\vec{K}_{pq} \cdot (\vec{K}_{mn} - K_0\hat{\rho}_2)]}{K_{rs} \cos\phi_0 \sqrt{\vec{K}_{mn} \cdot (\vec{K}_{mn} - 2K_0\hat{\rho}_2)}} \tag{3.30}$$

Here $K_{rs} = 2K_0 \cos\phi_0$ as dictated by the delta function in (3.27).

The corresponding symmetricized monostatic result given by Walsh *et al.* [69] is

$$\Gamma_{EP} = \frac{-j\left|\vec{K}_1 \times \vec{K}_2\right|^2}{2K^2\sqrt{\vec{K}_1 \cdot \vec{K}_2}} \tag{3.31}$$

where $K = 2K_0$, and $\vec{K}_1$, $\vec{K}_2$ are equal to $\vec{K}_{mn}$ and $\vec{K}_{pq}$, respectively. Equations (3.30) and (3.31) appear to be different from each other, but in fact they can be proven equivalent.

It is easy to see from the patch scatter geometry (Figure 3.2) that

$$\hat{\rho}_2 = \hat{x}\cos\theta_2 + \hat{y}\sin\theta_2 \tag{3.32}$$

can be written as

$$\hat{\rho}_2 = \hat{N}\cos\phi_0 + \hat{\theta}_N \sin\phi_0 \tag{3.33}$$

where the unit normal $\hat{N}$ and its orthogonal angular counterpart $\hat{\theta}_N$ may be written as

$$\begin{aligned} \hat{N} &= \hat{x}\cos(\theta_2 + \phi_0) + \hat{y}\sin(\theta_2 + \phi_0) \\ \hat{\theta}_N &= -\hat{x}\sin(\theta_2 + \phi_0) + \hat{y}\cos(\theta_2 + \phi_0) \end{aligned} \tag{3.34}$$

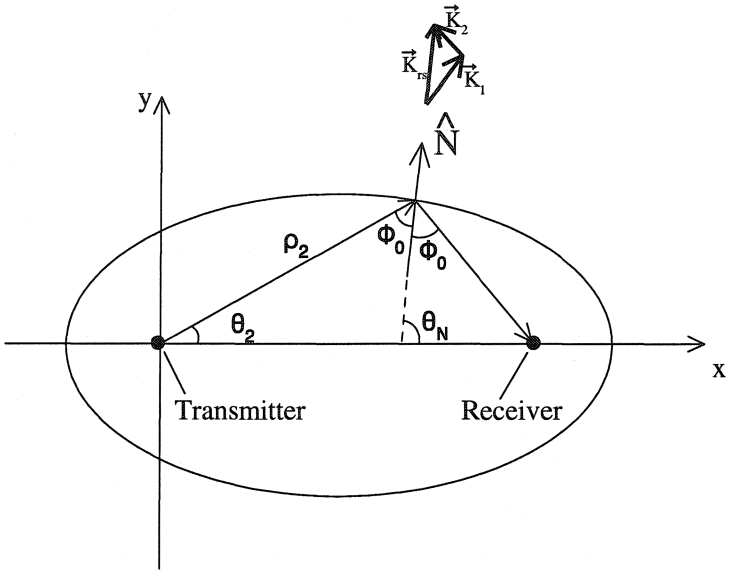

Figure 3.2: Depiction of the geometry associated with the second-order stationary phase condition.

For backscattering ($\phi_0 = 0$) and

$$\hat{\rho}_2 = \hat{N} \tag{3.35}$$

Also, for $\phi_0 = 0$, $\vec{K}_{rs} = 2K_0 \cos\phi_0 \hat{N} = 2K_0\hat{N}$. To conform to the monostatic analysis [69], we now set

$$\vec{K}_{rs} = \vec{K} = 2K_0\hat{N} \tag{3.36}$$

from which, using (3.34), we have

$$\hat{\rho}_2 = \hat{N} = \frac{\vec{K}}{2K_0} = \hat{K} \tag{3.37}$$

Furthermore,

$$\vec{K}_{mn} + \vec{K}_{pq} = \vec{K}_1 + \vec{K}_2 = 2K_0\hat{K} \tag{3.38}$$

Substituting (3.37)–(3.38) and $\phi_0 = 0$ into (3.30),

$$\begin{aligned}
\Gamma_{EP} &= \frac{-(\vec{K}_1 \cdot \hat{K})[\vec{K}_2 \cdot (\vec{K}_1 - K_0\hat{K})]}{K\sqrt{\vec{K}_1 \cdot (\vec{K}_1 - 2K_0\hat{K})}} \\
&= \frac{-(\vec{K}_1 \cdot \vec{K})[\vec{K}_2 \cdot (2\vec{K}_1 - 2K_0\hat{K})]}{2K^2\sqrt{\vec{K}_1 \cdot (-\vec{K}_2)}} \\
&= \frac{-[\vec{K}_1 \cdot (\vec{K}_1 + \vec{K}_2)][\vec{K}_2 \cdot (\vec{K}_1 - \vec{K}_2)]}{j2K^2\sqrt{\vec{K}_1 \cdot \vec{K}_2}} \\
&= \frac{j[{K_1}^2 + K_1K_2\cos(\theta_{\vec{K}_1} - \theta_{\vec{K}_2})][K_1K_2\cos(\theta_{\vec{K}_1} - \theta_{\vec{K}_2}) - {K_2}^2]}{2K^2\sqrt{\vec{K}_1 \cdot \vec{K}_2}} \\
&= \frac{j{K_1}^2{K_2}^2[\cos(\theta_{\vec{K}_1} - \theta_{\vec{K}_2})^2 - 1]}{2K^2\sqrt{\vec{K}_1 \cdot \vec{K}_2}} \\
&\quad + \frac{jK_1K_2\cos(\theta_{\vec{K}_1} - \theta_{\vec{K}_2})({K_1}^2 - {K_2}^2)}{2K^2\sqrt{\vec{K}_1 \cdot \vec{K}_2}} \\
&= \frac{-j\left|\vec{K}_1 \times \vec{K}_1\right|^2}{2K^2\sqrt{\vec{K}_1 \cdot \vec{K}_2}} + \frac{j\vec{K}_1 \cdot \vec{K}_2({K_1}^2 - {K_2}^2)}{2K^2\sqrt{\vec{K}_1 \cdot \vec{K}_2}}
\end{aligned} \tag{3.39}$$

Using the general "symmetricized" vector identity

$${}_s\Gamma_{EP}(\vec{K}_1, \vec{K}_2) = \frac{\Gamma_{EP}(\vec{K}_1, \vec{K}_2) + \Gamma_{EP}(\vec{K}_2, \vec{K}_1)}{2} \tag{3.40}$$

in (3.39) the coupling coefficient becomes

$${}_s\Gamma_{EP} = \frac{-j\left|\vec{K}_1 \times \vec{K}_2\right|^2}{2K^2\sqrt{\vec{K}_1 \cdot \vec{K}_2}} \tag{3.41}$$

which is identical to (3.31).

Therefore, the bistatic radar cross section equation (3.24) and the electromagnetic coupling coefficient (2.64) have been shown to properly reduce exactly to the monostatic model when $\phi_0 = 0$ is used in the former.

In this chapter, the time-dependant second-order normal E-field for bistatic HF radar patch scatter from a time-invariant surface has been extended to the ocean surface which is random and nonlinear. The second-order bistatic HF radar cross section of the ocean surface patch scatter has been developed by treating the Fourier coefficients in the series representing the surface as random variables, and the newly-derived result has also been verified.

Chapter 4

Simulation and Interpretation of Cross Section

One of the chief uses of HF radar is to extract sea surface parameters such as wind field, wave information and current field from the measured radar cross section spectrum. Thus, some of the basic properties of the HF radar cross section resulting from ocean surface patch scatter should be demonstrated. In this chapter, based on a parametric model for the ocean wave spectrum, the bistatic first- and second-order radar cross sections are computed and plotted. While it is simple to simulate the effects of ocean surface currents by adding appropriate Doppler shifts to the results, this is not done here.

4.1 Simulation Model

The HF radar sea echo Doppler spectrum can be simulated given the ocean wave spectrum model, radar operating frequency and ocean state parameters [76].

Any kind of ocean wave spectrum model may be used for the simulation. The most widely used one consists of the product of a one-dimensional (1-D) magnitude spectrum $S(K)$ and a directional factor $g(\theta_{\vec{K}})$:

$$S(\vec{K}) = S(K, \theta_{\vec{K}}) = S(K)g(\theta_{\vec{K}}) \tag{4.1}$$

where $\theta_{\vec{K}}$ is the dominant direction of the waves whose wavenumber is K. Here, the Pierson-Moskowitz nondirectional spectrum [77] is chosen for the 1-D wave spectrum $S(K)$. It assumes a fully developed wind-driven sea and has the form

$$S(K) = \frac{0.0081}{4K^4} \exp\left[-0.74\left(\frac{g}{KU_W^2}\right)^2\right] \tag{4.2}$$

in which U_W represents the wind speed 19.5 m above the ocean surface. This model is only good for a wind-driven sea when wind speed is no more than 20 m/s [77].

A cardioid directional distribution model proposed by Longuet-Higgins *et al.* [78] for $g(\theta_{\vec{K}})$ can be written as

$$g\left(K, \theta_{\vec{K}}\right) = F(s(K)) \cos^{(2s(K))}\left[\frac{\theta_{\vec{K}} - \varphi_W}{2}\right] \tag{4.3}$$

with $\theta_{\vec{K}}$ being the direction of the wave of wave vector $\vec{K}$, $s(K)$ representing the spreading parameter, and φ_W being the overall mean wind direction responsible for spectral growth. The factor F is a normalization imposed to make

$$\int_{-\pi}^{\pi} g\left(K, \theta_{\vec{K}}\right) d\theta_{\vec{K}} = 1 \tag{4.4}$$

and is given by

$$F(s(K)) = \frac{2^{(2s(K)-1)}\Gamma^2(s(K)+1)}{\pi\Gamma(2s(K)+1)} \tag{4.5}$$

where, in general, s is a function of wavenumber K and may be determined from [1] as

$$s(K) = 11.5\left(\frac{1}{U_{10}}\sqrt{\frac{g}{K}}\right)^{2.5} . \tag{4.6}$$

In (4.5), Γ is the usual gamma function, while in (4.6) U_{10} is the wind speed 10 m high over the sea surface. Also, (4.5) holds for $K > K_p$ where K_p is the peak of a Pierson-Moskowitz shape spectrum and the K here is taken to be that producing the maximum in equation (1.2).

While, in reality, both s and φ_W are functions of wavenumber K [79], [80], as is commonly done for simplicity, both s and φ_W will be modeled as constant over wavenumber in the following simulation. Here $s = 2$ is assumed, and then $F = 4/(3\pi)$, so that

$$g(\theta_{\vec{K}}) = \frac{4}{3\pi}\left|\cos^4\left(\frac{\theta_{\vec{K}} - \varphi_W}{2}\right)\right| \tag{4.7}$$

Given the above model and using particular values of wind speed and direction, radar frequency, and bistatic angle, equation (3.24) or (3.28) can be used to compute the second-order bistatic radar cross section normalized to patch area similar to that in [53]. Furthermore, the first-order bistatic radar cross section can be computed from (1.2). For this purpose, a typical radial patch width of $\Delta\rho_s$ =2000 m is used here.

4.2 Bistatic Cross Section Analyses

The bistatic second-order HF radar cross sections for patch scatter are computed and plotted for different sea state parameters as specified in the following sections, and the effects of these parameters on the radar cross sections are also analyzed.

4.2.1 The Effects of Wind Speed

Obviously, the wind-driven ocean wave spectrum is a function of wind speed in (4.2). According to equation (3.24) or (3.28), the radar cross sections are functions of the wave spectrum. Thus, it is clear that the wind speed will affect the radar cross section.

Figure 4.1 shows cross section results for an operating frequency of 25 MHz, wind direction of 180°, an ellipse normal angle of 90°, patch width of 2 km, and a transmitted pulse width of 13 μs. The wind direction is referenced to the x axis. The bistatic angle is taken to be 30°. The cross sections are plotted on a decibel scale.

In Figure 4.1, it might be noted that the magnitudes of second-order bistatic Doppler spectra adjacent to the first-order (Bragg) peaks are very sensitive to the change of wind speed. This reflects the fact that long ocean waves whose radar signatures are found in this Doppler region will carry a significant amount of spectral energy at higher wind speeds. Thus, the second-order Doppler spectra in this near-Bragg portion are very important in the process of inverting the cross sections in order to extract ocean surface state parameters such as the non-directional wave spectrum, wave height and wind speed (see, for example, [16], [23], [26], [33], [34], [48]).

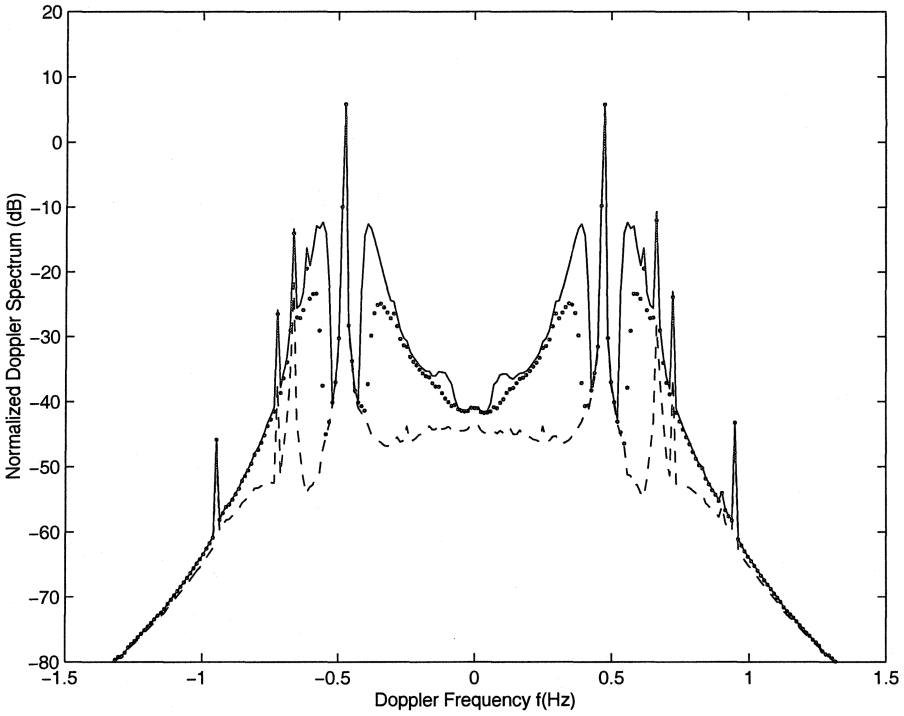

Figure 4.1: Bistatic patch scatter Doppler spectra under different wind speeds with wind direction of 180°. Wind speed is 15 m/s (solid line), 10 m/s (dotted line), and 5 m/s (dashed line).

The high-Doppler tails don't change significantly with wind speed. This is because the ocean waves responsible for the scattering associated with this portion of the Doppler spectrum lie in the saturated region of the Pierson-Moskowitz ocean wave spectrum where the spectral energy is almost independent of wind speed. Furthermore, for the same reason, the strengths of the bistatic Bragg peaks for the 25 MHz operating frequency are also insenstive to the wind speed change.

4.2.2 The Effects of Wind Direction

At HF, the Bragg waves are short enough to respond quickly to changes in the local wind conditions. The ratio of the intensities of the positive and negative peaks

is highly sensitive to the wind direction. Taking a monostatic radar system for example, if the wind is perpendicular to the radar beam direction for a significant period of time, the Bragg peaks will carry similar amounts of energy. In the other extreme, the negative/positive Bragg peak will be enhanced when the wind direction is parallel/antiparallel to the radar beam direction. The same is true for bistatic operation provided the reference is taken with respect to the scattering ellipse normal rather than the radar beam direction. The ratio of the approaching to receding Bragg energy is indicative of the (ambiguous) wind direction. This may be considered with reference to the directional distribution of the ocean wave energy. The distribution first proposed by Longuet-Higgins *et al.* [78] is expressed in (4.3).

In keeping with Stewart and Barnum [9] and taking monostatic radar as an example, a ratio R of the absolute strength of the approaching and receding Bragg peak energies B^+ and B^-, respectively, is given by

$$R = 10 \log \left(\frac{B^+}{B^-} \right) \tag{4.8}$$

Although external noise may contaminate B^+ and B^-, if it can be assumed that the noise spectral density is flat, there will be no effect on R. When s and F are assumed as constants over wavenumber, (4.3) simplifies to (4.7). Then, as in [9], R may be written as

$$R = 10 \log \left[\tan^{2s} \left(|\theta_W| / 2 \right) \right] \tag{4.9}$$

where s is a constant spreading factor, and θ_W is the angle between the radar beam direction and the mean wind direction. It should be noted that the logarithm ratio of the right Bragg peak to the left one has a theoretical limit of infinity, which

occurs when the wind direction is parallel to the radar beam. In practice, the limit can be large but not infinite and when R is more than 25 dB, the wind direction is assumed to be parallel with the radar beam. For a given R, θ_W is obviously given from equation (4.9) as

$$|\theta_W| = 2\tan^{-1}\left(10^{R/20s}\right) \tag{4.10}$$

or

$$\varphi_W = \theta_0 \pm |\theta_W| = \theta_0 \pm 2\tan^{-1}\left(10^{R/20s}\right) \tag{4.11}$$

where θ_0 is the radar beam direction. In (4.11), the $\pm$ indicates the ambiguity in the deduced wind direction. In other words, when wind direction is $\theta_0 + 2\tan^{-1}\left(10^{R/20s}\right)$ or $\theta_0 - 2\tan^{-1}\left(10^{R/20s}\right)$, the first-order echo has same characteristics. For illustrative purposes, $g(K, \theta_{\vec{K}})$ (normalized by F) for an operating frequency of 7.5 MHz, a wind speed of 11.2 m/s (i.e. $s(K) = 2$) and a dominant direction of $\varphi_W = 45°$ is plotted in Figure 4.2. For the radar look direction indicated, the ratio of OP to OP' would be the ratio of the Bragg peak energies. Of course, for a monostatic radar, this ratio would be the same for $\varphi_W = \theta_0 + \theta_W$. Hence, the usual directional ambiguity exists.

For the bistatic case, directional ambiguity still exists but with respect to the angle between wind direction and ellipse normal direction. Figure 4.3. gives the bistatic cross sections under different wind directions with a constant wind speed of 15 m/s. The normal to the scattering ellipse is 90°, other parameters are same as those in Figure 4.1. The wind direction, φ_W, is measured counterclockwise from the positive x-axis. It is clear that the relative strength ratio of the Bragg peaks depends on the wind direction. When the wind is perpendicular to the

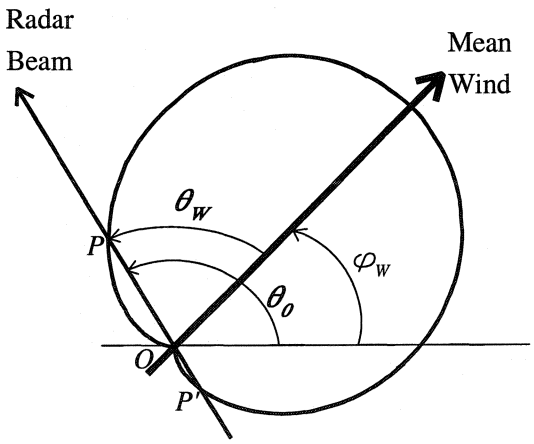

Figure 4.2: Wind directional distribution in relation to the radar look direction. The ratio of OP to OP' is indicative of the energy ratio of the spectral peaks associated with the receding to approaching Bragg waves.

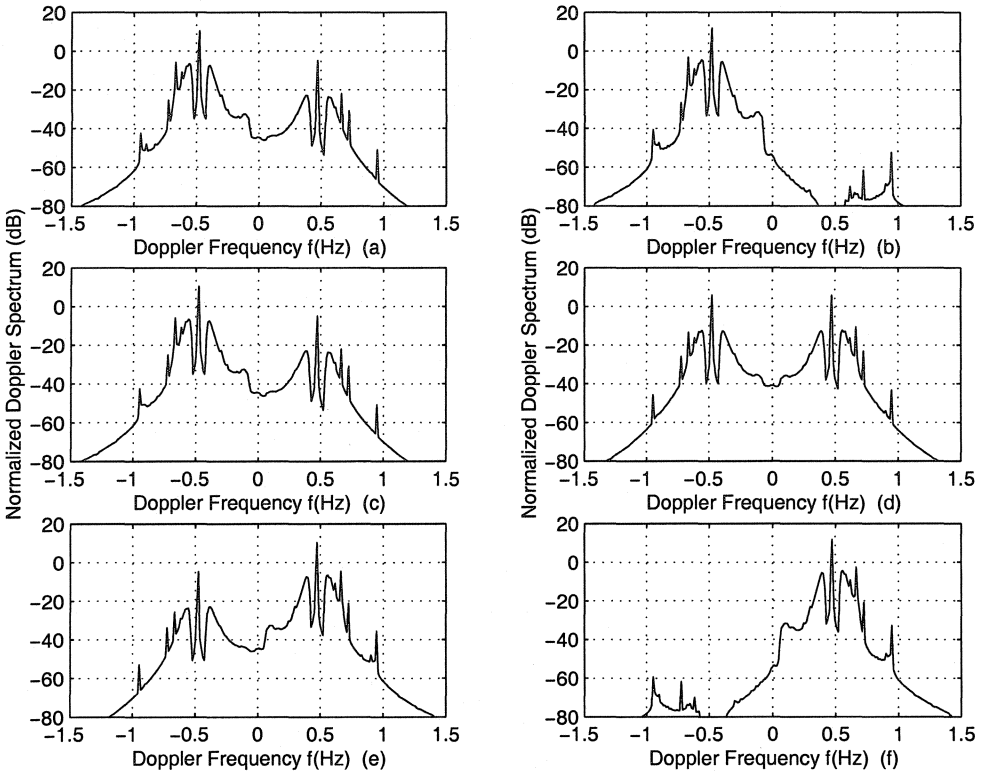

Figure 4.3: Bistatic patch scatter Doppler spectra under different wind directions with wind speed of 15 m/s. The wind direction is (a) 45°; (b) 90°; (c) 135°; (d) 180°; (e) 225°; (f) 270°.

ellipse normal direction, the Bragg peaks are equal and the Doppler spectrum is symmetric about zero Doppler shift. Otherwise, the negative/positive Bragg peak will be enhanced when the wind direction is parallel/antiparallel to the ellipse normal direction. Also, the antisymmetry that exists when wind direction changes from φ_W to $\varphi_W + 180°$ is obvious.

4.2.3 The Effects of Operating Frequency

While the analysis here is suitable for the entire HF band, different frequencies are employed for particular purposes. If shorter distance but better resolution are

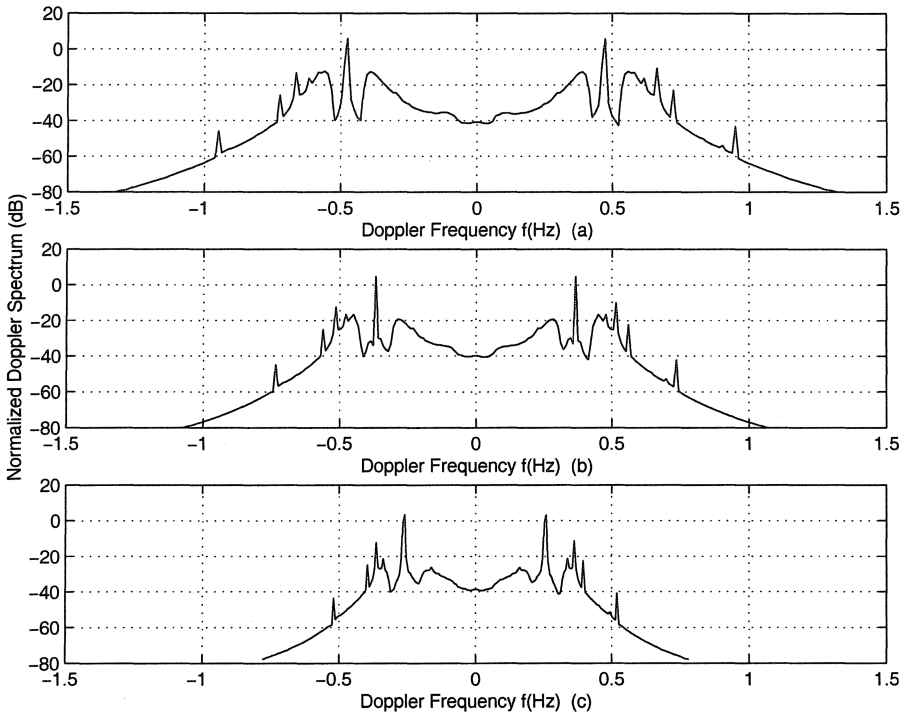

Figure 4.4: Bistatic patch scatter Doppler spectra for different operating frequencies with wind direction of 0° and wind speed of 15 m/s. The radar frequency is (a) 25 MHz; (b) 15 MHz; (c) 7.5 MHz.

required, the upper HF band should be used. This is because the propagation loss of radio waves increases at higher frequencies and radio signal with shorter wavelength can match shorter ocean waves or targets. When range is the main consideration, the lower HF band will be suitable, but then resolution is sacrificed. Thus, the effects of different operating frequencies on cross sections ought to be considered. Figure 4.4 gives the cross sections under three different operating frequencies. Other parameters are the same as those in Figure 4.1.

It is seen that the Bragg peaks' strengths don't change significantly when operating frequency varies. This is because for a 15 m/s wind speed the Bragg waves essentially lie in the saturated region of the Pierson-Moskowitz ocean wave

spectrum. However, the positions of the Bragg peaks shift in the Doppler spectrum as the operating frequency changes. This is obvious from the relationship [53]

$$f_B = 0.102\sqrt{f_0 \cos\phi_0} \tag{4.12}$$

where the unit of radar frequency f_0 is MHz. When f_0 becomes lower, the Bragg frequency f_B will be smaller, so the Bragg peaks are closer to zero Doppler shift.

For the second-order Doppler spectra, the near-Bragg amplitudes increase when the operating frequency goes up. This is because radio waves with shorter wavelengths can detect shorter ocean waves so that more information will be collected by the radar.

4.2.4 The Effects of Bistatic Angle

Clearly, when the geometry of a bistatic radar is established, the bistatic angles vary as the position of the scattering patch changes (see Figure 2.3). Thus, the effect of bistatic angle variation on the radar cross section is of interest. Figure 4.5. shows the cross sections under three different bistatic angles. Other parameters are the same as those in Figure 4.1.

From equation (4.12), it is known the Bragg Doppler frequency f_B is related to the bistatic angle ϕ_0. Thus, the positions of Bragg peaks shift in the Doppler spectrum with the bistatic angles. According to equation (4.12), when the bistatic angle ϕ_0 becomes closer to 90°, the Bragg frequency f_B will be smaller, and the Bragg peaks are closer to zero Doppler shift.

Meanwhile, the strengths of both first- and second-order Doppler spectra decrease when the bistatic angle is closer to 90°. From (4.12), it is easy to see that

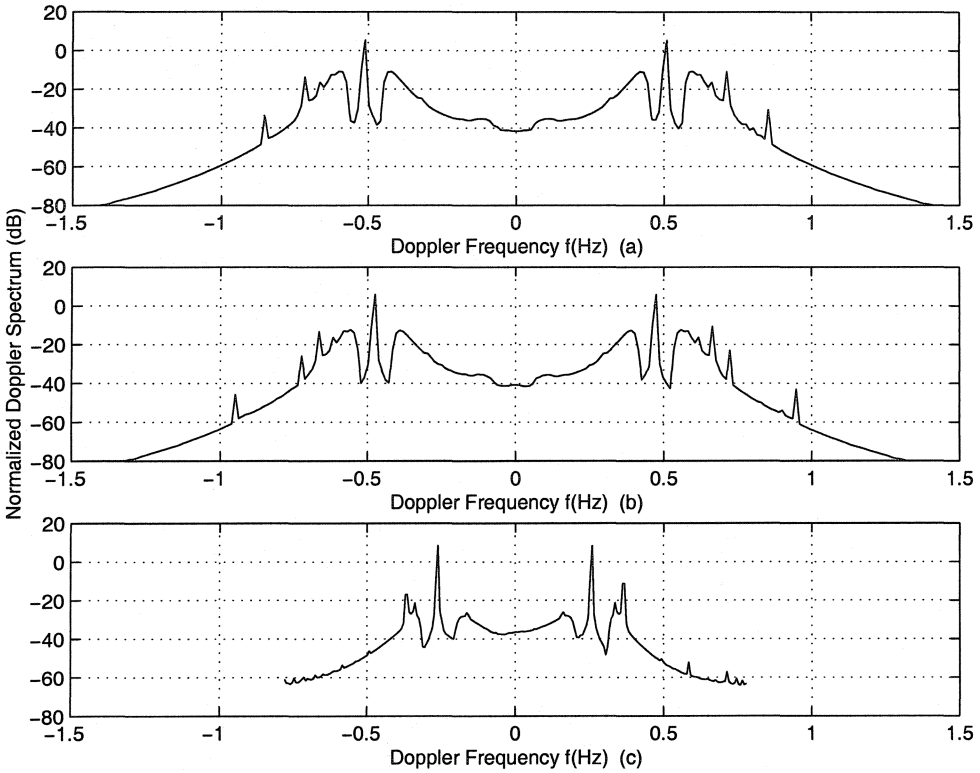

Figure 4.5: Bistatic patch scatter Doppler spectra for different bistatic angles with wind direction of 0° and wind speed of 15 m/s. The bistatic angle is (a) 0°; (b) 30°; (c) 75°.

the Bragg wave frequency $f_B \rightarrow 0$ as the bistatic angle $\phi_0 \rightarrow 90°$ (the scatter patch lies on the line defined by the transmitter and the receiver positions). The condition of $f_B \rightarrow 0$ means the Bragg wavelength $\lambda_B \rightarrow \infty$. The spectral energy will be small for such a wave, and so will be the resulting Doppler spectrum. Gill [53] also explains this by showing the hydrodynamic coupling coefficient $\Gamma_H \rightarrow 0$ as $\phi_0 \rightarrow 90°$.

For a bistatic radar whose parameters are the same as those in Figure 4.1, the corresponding monostatic operation changes the bistatic angle ϕ_0 (30°) into zero (the receiver is co-located with the transmitter), and look direction θ_L is taken to

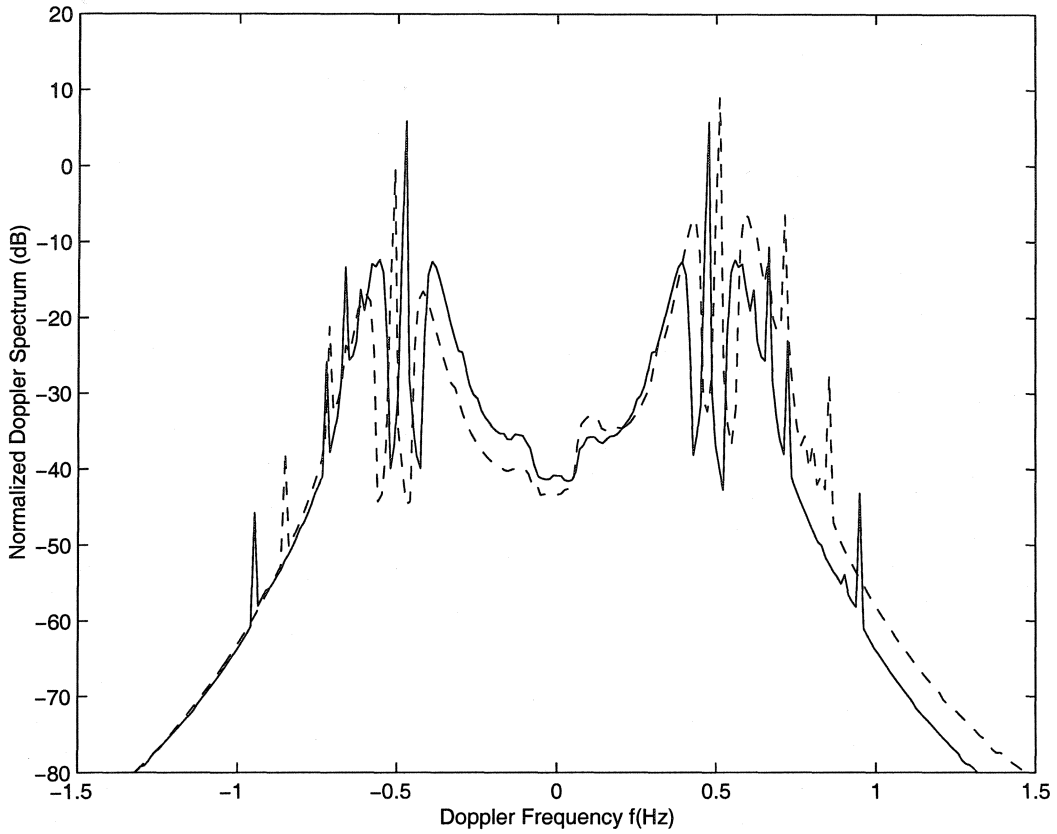

Figure 4.6: Comparison of bistatic (solid line) patch scatter Doppler spectra with monostatic (dashed line) result.

be 60°. Thus, the angle θ_W between the radar beam direction and the mean wind direction is 120°. Figure 4.6 shows the bistatic and monostatic results chosen for comparison. An operating frequency of 25 MHz, wind speed of 15 m/s, and wind direction of 180°, patch width of 2 km, and transmitted pulse width of 13 μs are assumed.

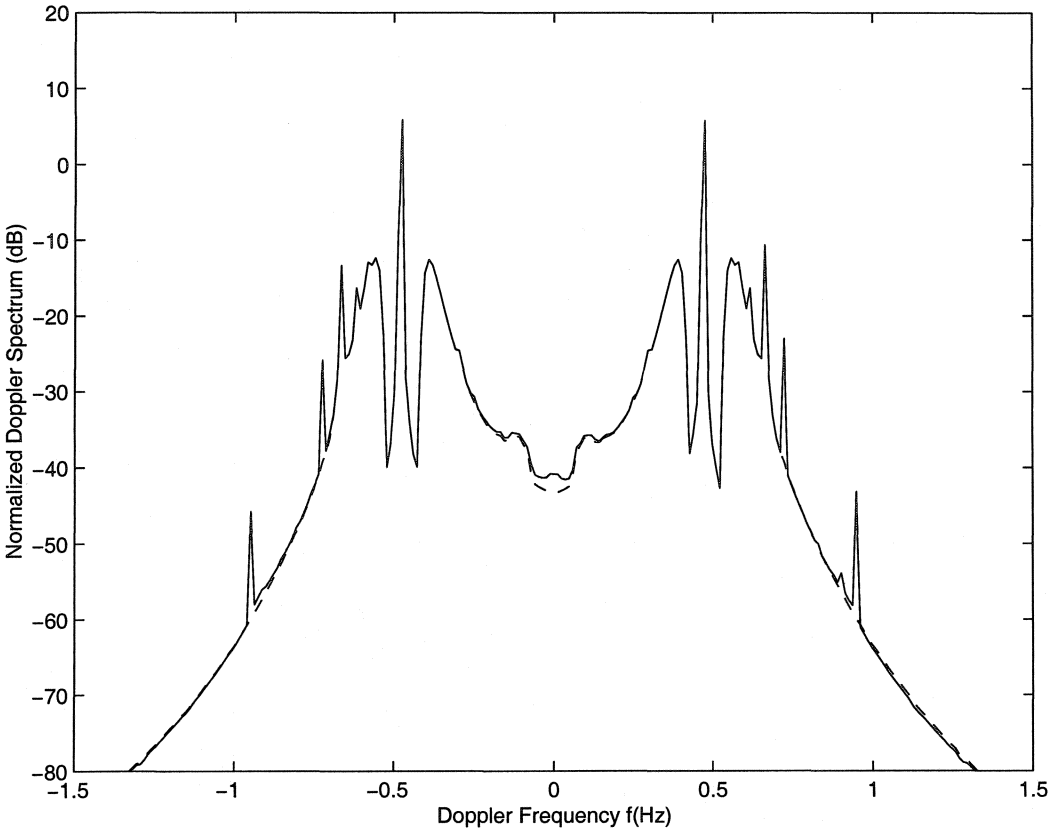

Figure 4.7: Comparison of bistatic patch scatter Doppler spectra (solid line) with the contribution of the hydrodynamic term only (dashed line).

4.2.5 The Effects of Coupling Coefficient

It has been pointed out that the total coupling coefficient includes the electromagnetic Γ_{EP} and hydrodynamic Γ_H effects. However, the hydrodynamic contribution dominates. This can be inferred from Figure 4.7 in which the combination of the electromagnetic and hydrodynamic contributions to the cross sections is compared to the hydrodynamic portion alone. Other radar parameters in Figure 4.7 are the same as those in Figure 4.1.

It can also be seen from the figure that the Doppler spectrum produced by

hydrodynamic nonlinear wave-wave interaction is very smooth and has no singularities, this can be explained from equation (3.7). The possible singularity can exist only when gK is equal to $(\omega_1 + \omega_2)^2$ in the denominator of the last term of (3.7). However, the angular frequency, $\omega(= \omega_1 + \omega_2)$, of the second-order wave is not related to the corresponding wavenumber, $K(\approx 2K_0 \cos\phi_0)$, via the linear dispersion relationship, so $gK = (\omega_1 + \omega_2)^2$ cannot be satisfied. However, there is one singularity on the Doppler spectrum including only the contribution of hydrodynamic coupling coefficient. This singularity comes from the Jacobian term of the integral transformation in equation (3.28). Gill [55] has shown that the singularity is at $\vec{K_1} = \vec{K_2} = (K_0 \cos\phi_0, \theta_N)$, and $\omega_d = \pm\sqrt{2} f_B$. This means the first-order waves responsible for the scattering at the singularity point have a wavenumber $K_0 \cos\phi_0$ which is half that of the bistatic Bragg wave. Thus, the wavelength λ of the scattering waves is twice that of the Bragg wave λ_B. Because the phase speed of first-order deep water wave is proportional to $\sqrt{\lambda}$ $(= \sqrt{2\lambda_B}$ here), the Doppler shift it produces is $\sqrt{2} f_B$. Meanwhile, a second-order wave which has a wave vector of $\vec{K} = \vec{K_1} + \vec{K_2} = (2K_0 \cos\phi_0, \theta_N)$, has a wavelength equal to λ_B. Since the speed of a second-order wave is $\sqrt{2}$ that of a first-order wave of the same wavelength, the second-order wave $\vec{K}$ will also produce a Doppler shift $\sqrt{2} f_B$. Thus, the $\sqrt{2} f_B$ peak in the Doppler spectrum arises from two first-order scatters from waves of length $2\lambda_B$ and a single scatter from a second-order wave of length λ_B. For the monostatic radar case ($\phi_0 = 0$), a similar result appears in [76].

From Figure 4.7, four more singularities can be seen on the complete bistatic patch scatter Doppler spectrum. These singularities come from the electromagnetic coupling coefficient. From equation (2.64), it is evident that the singularities

exist when $\vec{K_1} \cdot (\vec{K_1} - 2K_0\hat{\rho_2}) = 0$. Using the analysis found in [55], it can be shown that the singularities are at

$$f_d = \pm 2^{\frac{3}{4}} \sqrt{\frac{(1 \pm \sin\phi_0)^{\frac{1}{2}}}{\cos\phi_0}} f_B \tag{4.13}$$

when $K_1 = K_2$, $\theta_{\vec{K_1}} = \theta_N - (\frac{2\phi_0 \pm \pi}{4})$, $\theta_{\vec{K_2}} = \theta_N + (\frac{2\phi_0 \pm \pi}{4})$. For monostatic operation ($\phi_0 = 0$), the number of singularities reduces to two with $f_d = \pm 2^{\frac{3}{4}} (f_B)_{monostatic}$ which can be seen in Figure 4.6. This is the well-known "corner reflection" condition [76].

In this chapter, the bistatic radar cross sections for patch scatter have been simulated using the Pierson-Moskowitz model with a cardioid directional distribution for the directional ocean wave height spectrum of a wind-driven sea. Their properties and dependence on ocean conditions as well as on radar operating parameters have been depicted and analyzed.

Chapter 5

Conclusion

5.1 Summary

In previous theories for deriving radar cross sections, it is assumed that the scale of the illuminated area is infinite. However, the scale of the illuminated area is on the order of 1 km for the HF radar. Thus, the effect of the finite illuminated area (patch scatter) should be considered. In this thesis, the development of a model for the ocean patch scatter for bistatic radar is documented. It essentially involves the following steps: (1) finding and simplifying an expression for the second-order electric field equation for the bistatic reception of vertically polarized radiation scattered from a time-invariant rough surface derived by Walsh *et al.* [69]; (2) applying the solution to the ocean surface whose randomness may be introduced by treating the Fourier coefficients in the series representing the surface as random variables; (3) finding the autocorrelation of the total electric field expression (all relevant orders of scatter); (4) Fourier transforming the result to obtain the power spectral density; and (5) using the result from step (4) in the radar range equation

to get the cross section.

In this thesis, the two-dimensional spatial convolution electric field equation has been solved differently from Gill's method [54], [55], in which the inner convolution was calculated after its gradient. While Gill's approach [53] led to a more general result than previous investigators, it precluded the possibility of comparing the newly-derived bistatic patch-scatter cross sections with the monostatic counterpart already developed using the same theory [69]. Here, the inner convolution is calculated before its gradient. A bistatic HF radar cross section for patch scatter has been established but the electromagnetic coefficient is different from Gill's result [54], [55]. This difference comes from the different order of treating a gradient and convolution in the relevant electric field equation. The result allows direct comparison with existing monostatic models when the relevant geometry is introduced.

In developing the cross section, a pulsed dipole source is introduced into the second-order electric field equation. With small surface slope, small height and a vertical dipole source, a solution for the field equation is approximated via the stationary phase method. To make application to the ocean, a time-varying surface is introduced via a three-dimensional Fourier series with two spatial variables and one temporal variable. The Fourier transformation of the auto-correlations of the resulting fields gives the appropriate power spectral densities which are subsequently used in the bistatic radar range equation to produce the cross section.

The newly developed bistatic HF radar cross section for patch scatter has been verified in two ways: (1) the complete form of the bistatic HF radar cross section is shown to reduce to the proper monostatic models when the appropriate geometry for backscatter is introduced; (2) the electromagnetic coupling coefficient for the

bistatic case is seen to incorporate its monostatic counterpart.

Finally, the cross section model is also depicted and discussed based on simulation. The Pierson-Moskowitz non-directional ocean wave spectrum model with a cardioid directional distribution is used for the simulation. Some of the basic properties of the HF radar cross section spectrum resulting from ocean surface patch scatter have been demonstrated.

5.2 Future work

While, in fact, measured sea echo Doppler spectra are always contaminated to some extent by noise, this consideration is outside the scope of the work presented here. Future research should address this issue. Moreover, methods for extracting the sea surface state parameters already in existence and those currently being derived should be addressed using the new cross section. Simulated non-directional wave spectrum inversion results presented by Zhang *et al.* [81], [82] are encouraging and could be reanalyzed using the models developed in this thesis. Algorithms for the extraction of the ocean surface currents from the bistatic radar cross section are worthy of being studied. Future work is planned for field data to be obtained from the bistatic operation of radars on the Canadian East Coast. Additional research work should also include ionospheric effects on ocean patch scatter.

Bibliography

[1] H. Mitsuyasu, F. Tasai, T. Suhara, S. Mizuno, M. Onkusu, T. Honda, K. Rukiiski, "Observations of the directional spectrum of ocean waves using a cloverleaf buoy," *J. Phys. Oceanogr.*, vol. 5, pp. 750–760, 1975.

[2] Z. Wu, *Weather and the ocean*, Renminjiaotong Press, Beijing, 1982.

[3] E.D.R. Shearman, " Radio Science and Oceanography", *Radio Sci.*, vol. 18, no. 3, pp. 299–320, 1983.

[4] D.D. Crombie, "Doppler spectrum of sea echo at 13.56Mc/s", *Nature.*, vol. 175, no. 459, pp. 681–682, 1955.

[5] D.E. Barrick, "First-order theory and analysis of MF/HF/VHF scatter from the sea", *IEEE Trans. Antennas Propagat.*, vol. 20, no. 1, pp. 2–10, 1972.

[6] D. Barrick, "Remote sensing of sea state by radar", in *Remote Sensing of the Troposphere*, V.E. Derr, Ed., chapter 12, pp. 1–46. U.S. Government Printing Office, Washington, DC, 1972.

[7] J.F. Ward, "Power spectra from ocean movements measured remotely by ionospheric radio backscatter", *Nature*, vol. 223, pp. 1325–1330, 1969.

[8] A.E. Long and D.B. Trizna, "Mapping of north Atlantic winds by HF radar sea backscatter interpretation", *IEEE Trans. Antennas Propagat.*, vol. 21, no. 5, pp. 680–685, 1973.

[9] R.H. Stewart and J.R. Barnum, "Radio measurements of oceanic winds at long ranges: An evaluation", *Radio Sci.*, vol. 10, no. 10, pp. 853–857, 1975.

[10] J.R. Barnum, J.W. Maresca, and J.W. Serebreny, "High-resolution of oceanic wind fields with skywave radar", *IEEE Trans. Antennas Propagat.*, vol. 25, no. 1, pp. 128–132, 1977.

[11] J.W. Maresca and C.T. Carlson, "High-frequency skywave radar measurements of hurricane Anita", *Science.*, vol. 209, no. 4462, pp. 1189–1196, 1980.

[12] J.W. Maresca and J.R. Barnum, "Estimating wind speed from HF skywave radar sea backscatter", *IEEE Trans. Antennas Propagat.*, vol. 30, no. 5, pp. 846–852, 1982.

[13] J.W. Maresca and T.M. Geogres, "Measuring rms wave height and the scalar ocean spectrum with HF skywave radar", *J. Geophs. Res.*, vol. 85, no. C5, pp. 2759–2771, 1980.

[14] T.M. Geogres, "Progress toward a practical skywave sea-state radar", *IEEE Trans. Antennas Propagat.*, vol. 28, no. 6, pp. 751–761, 1980.

[15] T.M. Geogres, "Coastal ocean dynamics applications radar–a user's guide", Boulder Colo: NOAA Wave Propagation Lab, 1984.

[16] D.E. Barrick, "Extraction of wave parameters from measured HF radar sea-echo doppler spectra", *Radio Sci.*, vol. 12, no. 3, pp. 415–424, 1977.

[17] D.E. Barrick, M.W. Evans, and B.L. Weber "Ocean surface currents mapped by radar", *Science*, vol. 198, pp. 138–144, 1977.

[18] B. Lipa, "Derivation of directional ocean-wave spectra by integral inversion of second-order radar echoes", *Radio Sci.*, vol. 12, no. 3, pp. 425–434, 1977.

[19] D.E. Barrick, "EEZ surveillaince–the compact HF radar alternative", *EEZ Tech.*, vol. 3, pp. 125–129, 1998.

[20] S.J. Anderson, "Remote sensing with JINDALEE skywave radar", *IEEE J. Oceanic Eng.*, vol. 11, no. 2, pp. 158–163, 1986.

[21] S.J. Anderson, "HF skywave measurement of cyclone-generated ocean waves", *Proceedings of Radar Con-90.*, Adelaide, Australia, pp. 315–323, 1990.

[22] S.J. Anderson, "Adaptive remote sensing with HF skywave radar", *IEE Proc-F*, vol. 139, no. 2, pp. 182–92, 1992.

[23] P.E. Dexter and S. Theodorides, "Surface wind speed extraction from HF sky-wave radar doppler spectra", *Radio Sci.*, vol. 17, no. 3, pp. 643–652, 1982.

[24] J. Parent and C. Gaffard, "Detection of meteorological fronts over the North sea with Valesole skywave radar", *IEEE J. Oceanic Eng.*, vol. 11, no. 2, pp. 174–179, 1986.

[25] C. Gaffard and J. Parent, "Remote sensing of wind speed at sea surface level using HF skywave echoes from decemetric waves", *Geophys. Res. Lett.*, vol. 17, no. 5, pp. 615–618, 1990.

[26] L. Wyatt, "A relaxation method for integral inversion applied to HF radar measurements of ocean wave directional spectrum", *Int. J. Remote Sens.*, vol. 11, no. 8, pp. 1481–1494, 1990.

[27] L.R. Wyatt and L.J. Ledgard, "OSCR wave measurements – some preliminary results", *IEEE J. Oceanic Eng.*, vol. 21, no. 1, pp. 64–76, 1996.

[28] L.R. Wyatt, "The ocean wave directional spectrum", *Ocenaography.*, vol. 10, no. 2, pp. 85–89, 1997.

[29] L.R. Wyatt, "An evaluation of wave parameters measured using a single HF radar system", *Can. J. Remote Sensing*, vol. 28, no. 2, pp. 205–218, 2002.

[30] H.C. Graber and M.L. Heron, "Wave height measurement from HF radar", *Ocenaography.*, vol. 10, no. 2, pp. 90–92, 1997.

[31] H.C. Graber, B.K. Haus, L.D. Chapman, L.K. Shay, "HF radar comparison with moored estimates of current speed and direction: Expected differences and implications", *J. Geophys. Res.*, vol. 102, pp. 18749–18766, 1997.

[32] D.M. Fernanadez, H.C. Graber, and J.D. Paduan, "Mapping wind direction with HF radar", *Oceanography.*, vol. 10, no. 2, pp. 93–95, 1997.

[33] E. Gill and J. Walsh, "Extraction of ocean wave parameters from HF backscatter received by a four-element array: Analysis and application", *IEEE J. Oceanic Eng.*, vol. 17, no. 4, pp. 376–386, 1992.

[34] R. Howell and J. Walsh, "Measurement of ocean wave spectra using narrow beam HF radar", *IEEE J. Oceanic Eng.*, vol. 18, no. 3, pp. 296–305, 1993.

[35] R. Howell and J. Walsh, "Measurement of ocean wave spectra using a ship–mounted HF radar", *IEEE J. Oceanic Eng.*, vol. 18, no. 3, pp. 306–310, 1993.

[36] R. Howell and M. L. Khandekar, "Measuring ocean surface waves using HF ground wave radar–validation against a wave model", *Canadian J. Remote Sensing*, vol. 19, no. 1, pp. 102–109, 1993.

[37] K.J. Hickey, E.W. Gill, J.A. Helbig, and J. Walsh, "Measurement of ocean surface currents using a long-range, high-frequency ground wave radar", *IEEE J. Oceanic Eng.*, vol. 19, no. 4, pp. 549–554, 1994.

[38] E.W. Gill, M.L. Khandekar, R.K. Howell, and J. Walsh, "Ocean surface wave measurement using a steerable high frequency narrow beam ground wave radar", *J. of Atmos. Ocean. Technol.*, vol. 13, no. 3, pp. 703–713, 1996.

[39] S.F. Heron and R.J. Rose, "On the application of HF ocean radar to the observation of temporal and spatial changes in wind direction", *IEEE J. Oceanic Eng.*, vol. 11, no. 2, pp. 210–218, 1986.

[40] S.F. Heron and M.L. Heron, "A comparison of algorithms for extracting significant wave height form HF radar ocean backscatter spectra", *J. of Atmos. Ocean. Technol.*, vol. 15, no. 5, pp. 1157–1163, 1998.

[41] M.L. Heron and A. Prytz, "Wave height and wind direction from the HF coastal ocean surface radar", *Can. J. Remote Sensing.*, vol. 28, no. 3, pp. 385–393, 2002.

[42] Y. Hisaki, "Estimation of wave parameters and observation of two–dimensional current velocities by HF ocean radar", *J. Communication Res. Lab.*, vol. 40, no. 3, pp.133–139, 1993.

[43] Y. Hisaki, "Estimation of wave spectra using high–frequency ocean radar", *J. Communication Res. Lab.*, vol. 43, no. 3, pp. 375–379, 1996.

[44] Z. Zhou, Y. Liu, and J. Wang, "Surface wind field extraction from HF ground–wave remote sensing radar", in *Oceans Conference Record (IEEE)*, vol. 3, pp. 1488–1491, 1996.

[45] K.W. Gurgel, G. Antonischki, H.H. Essen, *et al*, "Wellen Radar (WERA): a new ground-wave HF radar for ocean remote sensing", *Coastal Eng.*, vol. 37, no. 3–4, pp. 219–234, 1999.

[46] W. Huang, S. Wu, B. Wen, J. Hou, "HF radar wind measurement over the Eastern China Sea", *Oceans, 2001, MTS/IEEE Conference and Exhibition*, vol. 1, pp. 642–645, 2001.

[47] W. Huang, *Research on ocean surface wind field and wave parameters with HF ground wave radar*, Ph.D. thesis, Wuhan University, Wuhan, China, 2001.

[48] W. Huang, S. Wu, E. Gill, B. Wen, J. Hou, "HF radar wind and wave measurement over the Eastern China Sea", *IEEE Trans. Geoscience Remote Sensing*, vol. 40, no. 9, pp. 1950–1955, 2002.

[49] J.F. Vesecky , J. Drake, C.C. Teague , F.L. Ludwig, K. Davidson, J Paduan, "Measurement of wind speed and direction using multifrequency HF radar", in *Proceedings of the Conference IGARSS*, Vol. 3, 1899–1901, 2002.

[50] J. Walsh and B. Dawe, "Development of a model for the first order bistatic ocean clutter radar cross section for ground wave radars", contract report, Northern Radar Systems Limited, 1994.

[51] J. Walsh, B. Dawe, and E. Gill, "An investigation of the first-order bistatic cross section of the ocean surface," in *Proc. IEEE Canadian Conference on Electrical and Computer Engineering*, St. Johns, Newfoundland, Canada, 1997.

[52] E. Gill and J. Walsh, "On the second-order high frequency bistatic ground wave radar cross section of the ocean surface", in *Proc. IEEE Canadian Conference on Electrical and Computer Engineering*, St. Johns, Newfoundland, Canada, vol. 2, pp. 516–519, 1997.

[53] E.W. Gill, "The scattering of high frequency electromagnetic radiation from the ocean surface: An analysis based on bistatic ground wave radar configuration", Ph.D. thesis, Mem. Univ. of Newfoundland, St. John's, Newfoundland, Canada, 1999.

[54] E.W. Gill and J. Walsh, "Bistatic form of the electric field equations for the scattering of vertically polarized high-frequency ground wave radiation from slightly rough, good conducting surfaces", *Radio Sci.*, vol. 35, no. 6, pp. 1323–1335, 2000.

[55] E.W. Gill and J. Walsh, "High-frequency bistatic cross sections of the ocean surface", *Radio Science.*, vol. 36, no. 6, pp. 1459–1476, 2001.

[56] D.B. Trizna, "A model for the first-order Doppler spectrum for bistatic HF radar surface wave sea scatter", in *Proceedings of the conference IGARSS*, pp. 7–11, 2001.

[57] D.B. Trizna, J. Gordan, H. Graber, B. Haus, "Result of a bistatic HF radar surface wave sea scatter experiment", in *Proceedings of the conference IGARSS*, Vol. 3, 1902–1904, 2002.

[58] J. Strutt, *The Theory of Sound*, vol. 2, Dover, Mineola, N.Y., 1945.

[59] S. Rice, "Reflection of electromagnetic waves from a slightly rough surface", *Theory of Electromagnetic Waves*, edited by K. Kline, pp. 351–378, Wiley-Interscience, New York, 1951.

[60] J. Wait, "Perturbation analysis for reflection from two–dimensional periodic sea waves", *Radio Sci.*, vol. 6, no. 3, pp. 378–391, 1971.

[61] D. Barrick, "Theory of HF and VHF propagation across the rough sea, 1, The effective surface impedance for a slightly rough highly conducting medium at grazing incidence", *Radio Sci.*, vol. 6, pp. 517–526, 1971.

[62] D. Barrick, "Theory of HF and VHF propagation across the rough sea, 2, Application to HF and VHF propagation above the sea", *Radio Sci.*, vol. 6, pp. 527–533, 1971.

[63] J. Walsh, "On the theory of electromagnetic propagation across a rough surface and calculations in the VHF region", *OEIC Rep. N00232*, Ocean Eng. Inf. Cent., Mem. Univ. of Newfoundland, St. John's, Newfoundland, Canada, 1980.

[64] J. Walsh and E.W. Gill, "An analysis of the scattering of high-frequency electromagnetic radiation from rough surfaces with application to pulse radar operating in backscatter mode", *Radio Sci.*, vol. 35, no. 6, pp. 1337–1359, 2000.

[65] E. Gill and J. Walsh, "A perspective on two decades of fundamental and applied research in electromagnetic scattering and high frequency ground wave radar on the Canadian East Coast", in *Proceedings of the Conference IGARSS*, Vol. 1, 521–523, 2002.

[66] J. Walsh and R. Donnelly, "A new technique for studying propagation and scattering for mixed paths with discontinuities", *Proc. R. Soc. Lond*, A412, pp. 125–167, 1987.

[67] J. Walsh and S. Srivastava, "Rough surface propagation and scatter, 1, General formulation and solution for periodic surfaces", *Radio Sci.*, vol. 22, no. 2, pp. 193–208, 1987.

[68] J. Walsh and R. Donnelly, "A consolidated approach to two-body electromagnetic scattering problems", *Phys. Rev. A Gen. Phys.*, vol. 36, no. 9, pp. 4474–4485, 1987.

[69] J. Walsh, R. Howell, and B. Dawe, "Model development for evaluation studies of ground wave radar", contract report 90-C14, Cent. for Cold Ocean Resour. Eng., Mem. Univ. of Newfoundland, St. John's, Newfoundland, Canada, 1990.

[70] S. Srivastava, "Analysis of HF scattering from an ocean surface: An alternative approach incorporating a dipole source", Ph.D. thesis, Mem. Univ. of Newfoundland, St. John's, Newfoundland, Canada, 1984.

[71] N. Beistein and R. Handelsman, "Asymptotic expansion of integrals", Holt, Rinehart, and Winston, Fort Worth, Tex., 1975.

[72] O. Phillips, *The Dynamics of the Upper Ocean*, Cambridge Univ. Press, New York, 1977.

[73] B. Kinsman, *Wind Waves*, Dover, Mineola, New York, 1984.

[74] B. Lathi, *Random Signals and Communication Theory*, Scranton, Penn: International Textbook Company, 1968.

[75] B.J. Lipa and D.E. Barrick, "Analysis methods for narrow-beam high-frequency radar sea echo", Technical Report ERL 420-WPL 56, National Oceanic and Atmospheric Administration, U.S. Department of Commerce, pp. 54, 1982.

[76] B. Lipa and D.E. Barrick, "Extraction of sea state from HF radar sea echo: Mathematical theory and modeling", *Radio Sci.*, vol. 21, no. 1, pp. 81–100, 1986.

[77] W.J. Pierson and L. Moskowitz, "A proposed spectral form for fully developed seas based upon the similarity theory of S.A. Kitaigorodskii", *J. Geophys. Res.*, vol. 69, no. 24, pp. 5181–5190, 1964.

[78] M.S. Longuet-Higgins, D.E. Cartwright, and N.D. Smith, "Observations of the directional spectrum of sea waves using the motion of a floation buoy", in *Proceedings of the Conference on Ocean Wave Spectra*, Prenticen-Hall Inc., Englewood Cliffs, N.J., pp. 111–136, 1963.

[79] M.L. Heron, "Applying a unified directional wave spectrum to the remote sensing of wind wave directional spreading", *Can. J. Remote Sensing*, vol. 28, no. 3, pp. 346–353, 2002.

[80] L. Wyatt and G.J. Holden. "Limits in direction and frequency resolution for HF radar ocean wave directional spectra measurement", *Global Atmosphere and Ocean System*, vol. 2, pp. 265–290, 1994.

[81] J. Zhang, "An algorithm for the extraction of ocean wave information from bistatic HF groundwave radar data – a simulation", M.E. thesis, Mem. Univ. of Newfoundland, St. John's, Newfoundland, Canada, 2003.

[82] E. Gill, W. Huang, and J. Zhang, "An alternate analysis for the second-order high frequency bistatic radar cross section of the ocean surface – patch scatter and its inversion", *Oceans, 2003, MTS/IEEE Conference and Exhibition*, pp. 2336–2340, 2003.

Appendix A

Method of Stationary Phase

Consider the complex integral

$$I = \int F(\alpha) e^{jZg(\alpha)} d\alpha \tag{A.1}$$

where Z is a large positive real number and $g(\alpha)$ and $F(\alpha)$ are complex functions of the complex variable α. $F(\alpha)$ is a slowly varying function of α.

The method of stationary phase is usually used when the integral is expressed in the form of (A.1). The stationary phase point $\alpha = \alpha_s$ is given by

$$\frac{\partial}{\partial \alpha}(g(\alpha)) = 0 \tag{A.2}$$

The integral is then evaluated to give

$$I \cong F(\alpha_s) e^{jZg(\alpha_s) + j\gamma \pm j(\pi/4)} \left[\frac{2\pi}{|g''(\alpha_s)|\, Z} \right]^{1/2} \tag{A.3}$$

where $''$ is the second-order derivative operator, and the constant γ is chosen such

that

$$[e^{j2\gamma}g''(\alpha_s)]$$

is real and positive (negative) for the upper (lower) sign in the exponent. Thus, if $g'' > 0$, $\gamma = 0$ and $+j\frac{1}{4}\pi$ must be used, and if $g'' < 0$, $\gamma = 0$ and $-j\frac{1}{4}\pi$ must be used.

For a two-dimensional integral,

$$I = \int\int F(\alpha,\beta)e^{jZg(\alpha,\beta)}d\alpha d\beta \tag{A.4}$$

the stationary phase point $\alpha = \alpha_s, \beta = \beta_s$ are given by

$$\begin{aligned} \frac{\partial g}{\partial \alpha} &= 0 \\ \frac{\partial g}{\partial \beta} &= 0 \end{aligned} \tag{A.5}$$

Then

$$I \cong \frac{1}{2}\left(\frac{2\pi}{Z}\right)\frac{F(\alpha_s,\beta_s)e^{jZg(\alpha_s,\beta_s)+j\frac{\pi}{4}Sig(g_{\alpha\beta}(\alpha_s,\beta_s))}}{\sqrt{|\det(g_{\alpha\beta}(\alpha_s,\beta_s))|}} \tag{A.6}$$

where $Sig(g_{\alpha\beta}(\alpha_s,\beta_s))$ =(number of positive eigenvalues)-(number of negative eigenvalues), and $\det(\cdot)$ means the determinant operator.

Appendix B

Radar Range Equation

The radar range equation provides an estimate of the received power spectral density from a particular target. The standard radar range equation for backscatter can be described as follows:

$$P_r(\omega_d) = \frac{\lambda_0^2 P_t G_t G_r |F(\rho)|^4}{(4\pi)^3(\rho)^4}\sigma(\omega_d) \tag{B.1}$$

where

λ_0 = The radar wavelength

P_t = Transmitted pulse (peak) power

$P_r(\omega_d)$ = Received power spectrum

G_t = Transmitting antenna gain

G_r = Receiving antenna gain

$F(\rho)$ = Rough spherical earth attenuation function

ρ = Range from the radar to the target

$\sigma(\omega_d)$ = Radar cross section as a function of Doppler frequency

ω_d = Doppler frequency

For bistatic radar, (B.1) should be modified as

$$P_r(\omega_d) = \frac{\lambda_0^2 P_t G_t G_r |F(\rho_1)F(\rho_2)|^2}{(4\pi)^3(\rho_1\rho_2)^2}\sigma(\omega_d) \tag{B.2}$$

where most of the terms have the same meaning as those in (B.1) except

ρ_1 = Range from the radar transmitter to the target

ρ_2 = Range from the radar receiver to the target

Appendix C

C++ Code for Simulation of Patch Scatter Cross Section

```
/*************************************************************
 *                                                           *
 *           BistaticPatchDOPPLER.cpp -- Simulate            *
 *           the patch scatter Doppler spectrum.             *
 *                                                           *
 *        simple integral with resolution of 0.025WB         *
 *                                                           *
 *                  Author: Weimin Huang                     *
 *                                                           *
 *************************************************************/

#include <conio.h>
#include <math.h>
```

```
#include <stdio.h>
#include <stdlib.h>
#define  PI  3.1415926535
#define  C   300000000   //velocity of light
#define  g   9.8

/*************************************************************
*                parameters notation                         *
*                                                            *
* Vp---input the wind velocity(m/s) 19.5m over the sea surface*
* f0---Radar operating frequency(MHz)                        *
* K0---radio wavenumber                                      *
* K1---the first ocean wavenumber                            *
* K2---the second ocean wavenumber                           *
* Wd---Doppler frequency                                     *
* WB---Bragg Doppler frequency                               *
* Q----Wind directon(degree)                                 *
* QN---direction of normal vector to the scattering ellipse  *
* Q0---half of the bistatic angle                            *
* Q1---the first ocean wave direction                        *
* Q2---the second ocean wave direction                       *
* s----spread factor                                         *
* ************************************************************/
```

```
  char fname[15];//filename for saving final results
  FILE *fd;

  double Vp,K0,K1,K2,K,Wd,WB,f0,Q,QN,Q0,Reso,cosQ2,K1p;
  double A=4/(3*PI),s=4;
  double h,p,DopVal[241],FirstOrder[241],DV,Val;
  int N,i,l,m,n=0;

void dif(double LowLimit,double UpLimit,int m1,int m2)
{
double Beta,Jd,Q1,Q2,Sigma,Sigma2,K_sqrt;
double fK_sqrt,fK_sqrtP,Gamma_E1,Gamma_E2,Gamma_ER,Gamma_EI;
double Gamma_E1R,Gamma_E1I,Gamma_H,Gamma_P;
int n3;
Sigma2=0.0;   //initialize the integral value
n3=m1*m2;
if(Wd>sqrt(2)*WB) Beta=acos(2*(WB/Wd)*(WB/Wd));
else Beta=0;
h=0.5*PI/180;  //integral step length of Theta=0.5 degree
Q1=LowLimit;//lower limit for integral

do
{
Sigma=0.0;  //initialize the integral value
```

```
/*************************************************************
*                                                           *
*       Newton's method for calculating ocean wavenumber K1   *
*                       for given Wd,Q1                     *
*                                                           *
*************************************************************/
    K_sqrt=0.00000001;// initial guess of K_sqrt=sqrt(K1)
do
{
if(K_sqrt<0) K_sqrt=-K_sqrt;
else K_sqrt=K_sqrt;
    fK_sqrt=Wd+sqrt(g)*(m1*K_sqrt
+m2*pow((pow(K_sqrt,4)+pow(2*K0*cos(Q0),2)
-4*K_sqrt*K_sqrt*K0*cos(Q0)*cos(Q1-QN)),0.25));
// ***fK_sqrt=Wd+m1*sqrt(g*K1)+m2*sqrt(g*K2)***
fK_sqrtP=sqrt(g)*(m1+m2*K_sqrt
*(K_sqrt*K_sqrt-2*K0*cos(Q0)*cos(Q1-QN))
*pow((pow(K_sqrt,4)+pow(2*K0*cos(Q0),2)
-4*K_sqrt*K_sqrt*K0*cos(Q0)*cos(Q1-QN)),-0.75));
// ***fK_sqrtP=derivative of fK_sqrt about K_sqrt***
        K_sqrt=K_sqrt-fK_sqrt/fK_sqrtP; //new value of K_sqrt
} while(fabs(fK_sqrt)>=0.0000001);
        K1=K_sqrt*K_sqrt; //first ocean wavenumber
```

```
/*****************************************************************
*                                                                *
*            Calculate K2, Q2 according to K1,Q1                 *
*                                                                *
*****************************************************************/
K2=pow((K1*K1+4*K0*K0*cos(Q0)*cos(Q0)
-4*K0*K1*cos(Q0)*cos(Q1-QN)),0.5);//second ocean wavenumber
cosQ2=(4*K0*K0*cos(Q0)*cos(Q0)
+K2*K2-K1*K1)/(4*K0*K2*cos(Q0));
if(fabs(cosQ2)<0.005) cosQ2=0;
else if(cosQ2>1.0) cosQ2=1;
     else if(cosQ2<-1.0) cosQ2=-1;
      else cosQ2=cosQ2;

        if((QN-PI)<=Q1&&Q1<=(QN-Beta)) Q2=QN+acos(cosQ2);
    else Q2=QN-acos(cosQ2);
/*****************************************************************
*                                                                *
*            Calculate Gamma_P,Jacobian,integral                 *
*                                                                *
*****************************************************************/
    Gamma_E1=K1*cos(Q1-QN+Q0)*(K2*K1*cos(Q1-Q2)
-K2*K0*cos(Q2-QN+Q0))/sqrt(fabs(K1*K1
-K1*2*K0*cos(Q1-QN+Q0)))/(2*K0*cos(Q0)*cos(Q0));
// ***Electromagnetic coupling coefficient Gamma_E(K1,K2)***
```

```
    if(K1*K1-K1*2*K0*cos(Q1-QN+Q0)>0.0)
{Gamma_E1R=-Gamma_E1;Gamma_E1I=0.0;}
    else{Gamma_E1I=Gamma_E1;Gamma_E1R=0.0;}
    Gamma_E2=K2*cos(Q2-QN+Q0)*(K1*K2*cos(Q2-Q1)
-K1*K0*cos(Q1-QN+Q0))/sqrt(fabs(K2*K2
-K2*2*K0*cos(Q2-QN+Q0)))/(2*K0*cos(Q0)*cos(Q0));
// ***Electromagnetic coupling coefficient Gamma_E(K1,K2)***
        if(K2*K2-K2*2*K0*cos(Q2-QN+Q0)>0.0)
{Gamma_ER=Gamma_E1R-Gamma_E2;Gamma_EI=Gamma_E1I+0.0;}
        else{Gamma_EI=Gamma_E1I+Gamma_E2;Gamma_ER=Gamma_E1R;}
    Gamma_H=0.5*(K1+K2+n3*sqrt(K1*K2)*(1-cos(Q1-Q2))*(g*2
*K0*cos(Q0)+(Wd)*(Wd))/(g*2*K0*cos(Q0)-(Wd)*(Wd)));
    /* Gamma_P=pow(Gamma_H,2); //for only hydrodynamic */
    Gamma_P=pow(Gamma_H+0.5*Gamma_ER,2)+pow(0.5*Gamma_EI,2);
// ***square of the patch scatter coupling coefficicent***
        Jd=sqrt(g)*(1+n3*(pow(K1,1.5)-2*sqrt(K1)*K0*cos(Q0)
*cos(Q1-QN))*pow(K1*K1+4*K0*K0*cos(Q0)*cos(Q0)
-4*K1*K0*cos(Q0)*cos(Q1-QN),-0.75)); //Jacobian term
    Jd=fabs(Jd);
    if(Jd>=0.001)Jd=pow(K1,1.5)*pow(Jd,-1);
    else Jd=1000000000000000;
    Sigma+=128*PI*PI*pow(K0,4)*pow(cos(Q0),4.0)*Gamma_P*Jd
*0.002025*A*pow(K1,-4)*exp(-0.74*g*g*pow(K1,-2)
*pow(Vp,-4))*pow(cos(((1-m1)/2*PI+Q1-Q)/2.0),s)
*0.002025*A*pow(K2,-4)*exp(-0.74*g*g*pow(K2,-2)
```

```
*pow(Vp,-4))*pow(cos(((1-m2)/2*PI+Q2-Q)/2.0),s);

/*************************************************************
*                                                           *
*            Calculate the contribution of K1>K2            *
*                                                           *
*************************************************************/
    K1p=K1;
        K1=K2;
    K2=K1p;
    K1p=Q1;
    Q1=2*QN-Q2;
    Q2=2*QN-K1p;
    if(m1==m2) {m1=m1;m2=m2;}
    else  {m1=-m1;m2=-m2;}

    Gamma_E1=K1*cos(Q1-QN+Q0)*(K2*K1*cos(Q1-Q2)
-K2*K0*cos(Q2-QN+Q0))/sqrt(fabs(K1*K1
-K1*2*K0*cos(Q1-QN+Q0)))/(2*K0*cos(Q0)*cos(Q0));
// ***Electromagnetic coupling coefficient Gamma_E(K1,K2)***
    if(K1*K1-K1*2*K0*cos(Q1-QN+Q0)>0.0)
{Gamma_E1R=-Gamma_E1;Gamma_E1I=0.0;}
    else{Gamma_E1I=Gamma_E1;Gamma_E1R=0.0;}
    Gamma_E2=K2*cos(Q2-QN+Q0)*(K1*K2*cos(Q2-Q1)
-K1*K0*cos(Q1-QN+Q0))/sqrt(fabs(K2*K2
```

```
-K2*2*K0*cos(Q2-QN+Q0)))/(2*K0*cos(Q0)*cos(Q0));
// ***Electromagnetic coupling coefficient Gamma_E(K1,K2)***
        if(K2*K2-K2*2*K0*cos(Q2-QN+Q0)>0.0)
{Gamma_ER=Gamma_E1R-Gamma_E2;Gamma_EI=Gamma_E1I+0.0;}
        else{Gamma_EI=Gamma_E1I+Gamma_E2;Gamma_ER=Gamma_E1R;}
    Gamma_H=0.5*(K1+K2+n3*sqrt(K1*K2)*(1-cos(Q1-Q2))*(g*2
*K0*cos(Q0)+(Wd)*(Wd))/(g*2*K0*cos(Q0)-(Wd)*(Wd)));
    Gamma_P=pow(Gamma_H,2); //for only hydrodynamic***
    // ***Gamma_P=pow(Gamma_H+0.5*Gamma_ER,2)+pow(0.5*Gamma_EI,2);
    Jd=sqrt(g)*(1+n3*(pow(K1,1.5)-2*sqrt(K1)*K0*cos(Q0)
*cos(Q1-QN))*pow(K1*K1+4*K0*K0*cos(Q0)*cos(Q0)
-4*K1*K0*cos(Q0)*cos(Q1-QN),-0.75));
    Jd=fabs(Jd);
    if(Jd!=0)Jd=pow(K1,1.5)*pow(Jd,-1);
    else Jd=0;
    Sigma+=128*PI*PI*pow(K0,4)*pow(cos(Q0),4.0)*Gamma_P*Jd
*0.002025*A*pow(K1,-4)*exp(-0.74*g*g*pow(K1,-2)
*pow(Vp,-4))*pow(cos(((1-m1)/2*PI+Q1-Q)/2.0),s)
*0.002025*A*pow(K2,-4)*exp(-0.74*g*g*pow(K2,-2)
*pow(Vp,-4))*pow(cos(((1-m2)/2*PI+Q2-Q)/2.0),s);

        Q1=K1p; //return the values for next integral
    if(m1==m2) {m1=m1;m2=m2;}
    else  {m1=-m1;m2=-m2;}
```

```
    Sigma=Sigma*h;
    Sigma2+=Sigma; //sum the integral
    Q1=Q1+h;
} while(Q1<=UpLimit);
DopVal[n]+=Sigma2; //array for storing the final integral
  }

void ModualDoppler()
{
  printf("input data filename(*.dpl)-->"); //input the
  // ***filename for saving the final results***
  scanf("%s",&fname);printf("\n");
  if((fd=fopen(fname,"wb"))==NULL)
  {
   printf("cannot open\n");
   exit(1);
  }

  // ***input the radar operating frequency(MHz)***
  printf("radar frequency f0(MHz)=  ");
  scanf("%lf",&f0);printf("\n");
  // ***input the wind velocity(m/s)***
  printf("wind speed V19.5(m/s)=  ");
  scanf("%lf",&Vp);printf("\n");
  // ***input the wind directon(degree)***
```

```
  printf("wind directin Q(degree)=  ");
  scanf("%lf",&Q);printf("\n");
  Q=Q*PI/180.0;
  // ***input the normal directon(degree)***
  printf("normal vector angle QN(degree)=  ");
  scanf("%lf",&QN);printf("\n");
  QN=QN*PI/180.0;
  // ***input the bistatic angle (degree)***
  printf("bistatic angle Q0(degree)=  ");
  scanf("%lf",&Q0);printf("\n");
  // ***input the resolution (m)***
  printf("range resolution P(m)=  ");
  scanf("%lf",&Reso);printf("\n");
  Q0=Q0*PI/180.0;
  K0=2*PI*f0/300;  //radio wavenumber
  WB=sqrt(2*g*K0*cos(Q0)); //Bragg radial frequency
/************************************************************
*                                                           *
*          Calculate the second-order cross section         *
*                                                           *
************************************************************/
  // ***calculating Doppler spectra by Doppler frequency***
  // ***for -3WB<Wd<-WB with step of 0.025WB***
  for(N=0;N<80;N++)
  {
```

```
Wd=(-3.0+0.025*N)*WB;
DopVal[N]=0.0;
if(Wd+sqrt(2.0)*WB>0)// for Wd>=-sqrt(2)*WB
{
if(N==64) Wd=-sqrt(2)*WB;//singularity at Wd=-sqrt(2)*WB
else;

if(fabs(Wd+pow(2,0.75)*sqrt(pow(1-sin(Q0),0.5)
/cos(Q0))*WB)<=0.0125*WB)
Wd=-pow(2,0.75)*sqrt(pow(1-sin(Q0),0.5)/cos(Q0))*WB;
// ***singularity from E coupling coefficient***
else;

    dif(QN-PI,QN,1,1);
dif(QN,QN+PI,1,1);
}
else // for Wd<-sqrt(2)*WB
{
if(fabs(Wd+pow(2,0.75)*sqrt(pow(1-sin(Q0),0.5)
/cos(Q0))*WB)<=0.0125*WB)
Wd=-pow(2,0.75)*sqrt(pow(1-sin(Q0),0.5)/cos(Q0))*WB;
// ***singularity from E coupling coefficient***
else;

if(fabs(Wd+pow(2,0.75)*sqrt(pow(1+sin(Q0),0.5)
```

```
 /cos(Q0))*WB)<=0.0125*WB)
 Wd=-pow(2,0.75)*sqrt(pow(1+sin(Q0),0.5)/cos(Q0))*WB;
 // ***singularity from E coupling coefficient***
     else;
     dif(QN-PI,QN-acos(2*(WB/Wd)*(WB/Wd)),1,1);
 dif(QN+acos(2*(WB/Wd)*(WB/Wd)),QN+PI,1,1);
 }
n++;
}
n++;

// ***calculating Doppler spectra for -WB<Wd<0 ***
for(N=81;N<120;N++)
{
 Wd=(-3+0.025*N)*WB;
 DopVal[N]=0.0;
 if(fabs(Wd+pow(2,0.75)*sqrt(pow(1-sin(Q0),0.5)
 /cos(Q0))*WB)<=0.0125*WB)
 Wd=-pow(2,0.75)*sqrt(pow(1-sin(Q0),0.5)/cos(Q0))*WB;
 // ***singularity from E coupling coefficient***
 else;
 dif(QN-PI,QN,-1,1);
 dif(QN,QN+PI,-1,1);
 n++;
}
```

```
if(N==120)// Wd=0
{
Wd=(-3+0.025*N)*WB;
    DopVal[N]=0.0;
    dif(QN-0.5*PI,QN+0.5*PI,-1,1);
    n++;
}
else;
N++;

// ***calculating Doppler spectra for 0<Wd<WB ***
for(N=121;N<160;N++)
{
 Wd=(-3+0.025*N)*WB;
 DopVal[N]=0.0;
 if(fabs(Wd-pow(2,0.75)*sqrt(pow(1-sin(Q0),0.5)
 /cos(Q0))*WB)<=0.0125*WB)
 Wd=pow(2,0.75)*sqrt(pow(1-sin(Q0),0.5)/cos(Q0))*WB;
 // ***singularity from E coupling coefficient***
 else;
 dif(QN-PI,QN,1,-1);// non-singularity but -0<Wd<WB
 dif(QN,QN+PI,1,-1);
  n++;
}
n++;
```

```
// ***calculating Doppler spectra for WB<Wd<3WB ***
for(N=161;N<=240;N++)
{
 Wd=(-3+0.025*N)*WB;
 DopVal[N]=0.0;
 if(Wd-sqrt(2.0)*WB<0)// for Wd<=sqrt(2)*WB
 {
 if(N==176) Wd=sqrt(2)*WB;// singularity at Wd=sqrt(2)*WB
 else;

 if(fabs(Wd-pow(2,0.75)*sqrt(pow(1-sin(Q0),0.5)
 /cos(Q0))*WB)<=0.0125*WB)
 Wd=pow(2,0.75)*sqrt(pow(1-sin(Q0),0.5)/cos(Q0))*WB;
 // ***singularity from E coupling coefficient***
 else;

  dif(QN-PI,QN,-1,-1);
  dif(QN,QN+PI,-1,-1);
 }
 else // for Wd>sqrt(2)*WB
 {

 if(fabs(Wd-pow(2,0.75)*sqrt(pow(1-sin(Q0),0.5)
 /cos(Q0))*WB)<=0.0125*WB)
```

```
    Wd=pow(2,0.75)*sqrt(pow(1-sin(Q0),0.5)/cos(Q0))*WB;
    // ***singularity from E coupling coefficient***
    else;

    if(fabs(Wd-pow(2,0.75)*sqrt(pow(1+sin(Q0),0.5)
    /cos(Q0))*WB)<=0.0125*WB)
    Wd=pow(2,0.75)*sqrt(pow(1+sin(Q0),0.5)/cos(Q0))*WB;
    // ***singularity from E coupling coefficient***
    else;
    dif(QN-PI,QN-acos(2*(WB/Wd)*(WB/Wd)),-1,-1);
        dif(QN+acos(2*(WB/Wd)*(WB/Wd)),QN+PI,-1,-1);
}
    n++;
  }

/*************************************************************
*                                                            *
*            Calculate the first-order cross section         *
*                                                            *
*************************************************************/
  for(N=0;N<=240;N++) //calculate first-order
  {
  FirstOrder[N]=0;
      for(l=0;l<10;l++)//find the max among ten data
  {
```

```
  if(N>120) m=-1;
  else m=1;
  K=pow((-3+0.0025*(N*10+l))*WB,2)/g;
  if(N==80||N==160) //for sin(x)/x when x=0
  Val=pow(2,4)*PI*pow(K0,2)
    *0.00405*A*pow(K,-4)
*exp(-0.74*g*g*pow(K,-2)*pow(Vp,-4))
*pow(cos(((1-m)/2*PI+QN-Q)/2.0),s)
*pow(K,2.5)*cos(Q0)/sqrt(g)*Reso
*pow(cos(Reso/2*(K/cos(Q0)-2*K0)),2);
  else
      Val=pow(2,4)*PI*pow(K0,2)
    *0.00405*A*pow(K,-4)
*exp(-0.74*g*g*pow(K,-2)*pow(Vp,-4))
*pow(cos(((1-m)/2*PI+QN-Q)/2.0),s)
*pow(K,2.5)*cos(Q0)/sqrt(g)*Reso
*pow(sin(Reso/2*(K/cos(Q0)-2*K0))
/(Reso/2*(K/cos(Q0)-2*K0)),2);
  if(Val>=FirstOrder[N]) FirstOrder[N]=Val;
  else;
 }
 }
 DopVal[120]=(DopVal[119]+DopVal[121])/2;
```

```
/*************************************************************
*                                                           *
*        Sum the first- and second-order and normalize      *
*                                                           *
//***********************************************************/
  // ***normalize Doppler spectra to -90dB---0dB ***
  for(N=0;N<=240;N++)
  {
       DopVal[N]=DopVal[N]+FirstOrder[N];
   if(DopVal[N]<=0.000000)
   DopVal[N]=-90.0;
   else
   DopVal[N]=10*log10(DopVal[N]);
   if(DopVal[N]<-90.0)
   DopVal[N]=-90.0;
   else if(DopVal[N]>5.000000)
   {
   if(N!=80&&N!=160)
   {
   DopVal[N]=DopVal[N-1]+15;
   if(DopVal[N]-DopVal[N-2]==30.000000)
   {
          DopVal[N]=DopVal[N]-15;
   }
   }
```

```
    else;

    }
    else;
    printf("%d,%e\n",N,DopVal[N]);
  }
  printf("You got 241 Doppler values successfully\n");

  //write final results to filename
  if(fwrite(DopVal,sizeof(double)*241,1,fd)!=1)
  printf("cannot write\n");
}

main()
{
ModualDoppler();
}
```